Chapter 1. Introduction

1-1. Energy and Photovoltaics

1-1.1 Brief Talk About the Energy Crisis and Renewable Energy

5 years ago, there is a movie named "**The Day After Tomorrow**" claimed that our beautiful world sooner or later might be destroyed by lots of catastrophes like storm, tsunami, tornado, earthquake, blizzard…etc. and those catastrophes simply come from "Atmospheric Greenhouse Effect" or" Global Warming". 3 years ago, there is another movie played by the Ex-Vice President of the US Al Gore named "**An Inconvenient Truth**" which exposes more incredible, unbelievable truths to the whole world.

The movie points out the critical problem we have and also gets more and more responses from people. The word "Global Warming" means both the average temperature of the Earth's near-surface air and oceans getting increase, actually, the temperature increased 0.74 ± 0.18 °C (1.33 ± 0.32 °F) during the last century.
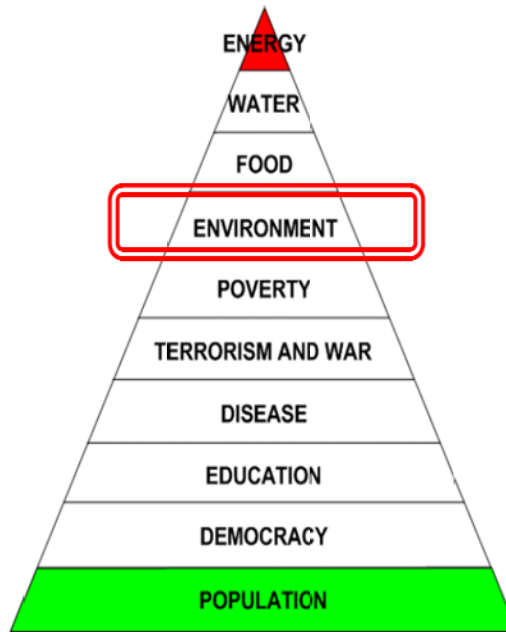
Fig.1.1 The 10 top crises of the world, energy is No.1 and even environment is
before top 5.

Global Warming is the most important issue for all countries, as the contents of

exhausted carbon dioxide increase every year even single day, the temperature of our

environment are getting higher. But why the carbon dioxide increase so rapidly? The

main reason is burning oil, coal, gas and so on. At the same time, the depletion of the

fossil fuels will occurs in about forty, two hundreds, sixty years respectively. That

brings all the mankind a serious problem, Fig.1.1 shows the 10 top crises of the globe,

people figure the trouble out so fast that they try to produce the alternative energy, and

solar energy is one of the well-known renewable energy, it's clean, plenty and easy to

get in everywhere that sunlight can reach even in the north pole and the south pole.

The first photovoltaic (also called solar cell) was studied at Bell Laboratories.

After that, in 1973, the oil crisis broke out on October 15, from that day on, people

recognized that solar energy might be a solution.

Till now, Si is known to be the second most abundant element (after oxygen) in the

earth's crust, making up 25.7% of the crust by mass. Pure silicon is used to produce ultra-pure silicon wafers used in the semiconductor industry, in electronics and in photovoltaic applications.

Ultra-pure silicon can be doped with other elements to adjust its electrical response by controlling the number and charge (positive or negative) of current carriers. Such control is necessary for transistors, **photovoltaics** (**solar cells**), integrated circuits, microprocessors, and other semiconductor devices which are used in electronics and other high-tech applications.

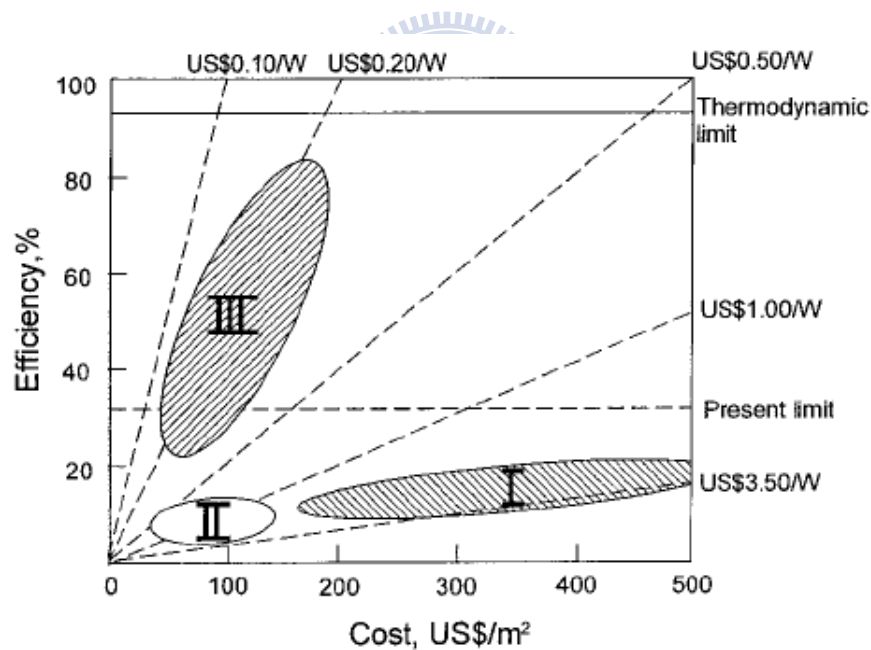## 1-1. 2 Comparisons Between Three Generation Photovoltaics

Fig.1.2 Efficiency and cost projections for first-, second- and third-generation

photovoltaic technology (wafers, thin-films, and advanced thin-films,

respectively) [1]

The vast majority of the **first generation photovoltaics** using silicon wafer as

materials, mainly due to the production of silicon solar cell manufacturing process and the principle is very close to the semiconductor industry, otherwise, the production technology and equipment of semiconductor industry have also been quite mature currently. The **first generation photovoltaics** mainly constructed by a single p-n junction, its theoretical limiting efficiency is about 31% [1], but in general, the conversion efficiency is about 17 in polycrystalline and 18 % in single crystalline (Motech) in modules.

Because the **first generation photovoltaics** are wafer-based, involving high energy and labor inputs which prevent any significant progress in reducing production costs as Fig.1.2 shows. In addition, the efficiency of the **first generation photovoltaics** seems to be encountering difficulties and bottleneck. When the supply shortage of silicon wafer material continued to widen, the need for the **second generation photovoltaics**, "thin film solar cells" has risen.

Second generation photovoltaics development mainly was directed against the production cost and energy requirement, so production costs could be reduced. Thin-film solar cells (**second generation**) depending on the type of materials can be divided into several categories: silicon thin film (amorphous silicon, hydrogenated amorphous silicon: (a-Si: H), microcrystalline silicon cell), **CdTe**, **CIGS** (CIS), GaAs multijunction.

At present, the conversion efficiency of thin-film solar cells is not as good as Si-based solar cells, but the Thin-film Solar Cell R & D Center want to combine the glass with building materials, to form the large-area thin-film solar cell glass building material, together with the advantages of cheap raw materials, can make large-scale

thin-film solar cell a better power generation.

The purpose of the **third generation photovoltaics** is to enhance poor electrical performance of the **second generation photovoltaics** and achieve low-cost productions at the same time. The goal of third generation conversion efficiency is > 31% even higher, while maintaining low-cost materials. Another consideration of the third generation photovoltaics is that it focuses on materials which do not have toxicity.

There are several ways to achieve such high conversion efficiency, including Dye-sensitized solar cells (DSSC), Organic/polymer solar cells [**2**], the use of multilayer photovoltaic cells or so called Tandem Cells, Hot Carrier Cells, Multi electron-hole pairs, Multiband and Impurity Photovoltaic Cells, Thermophotovoltaic and Thermophotonic Devices [**3**].
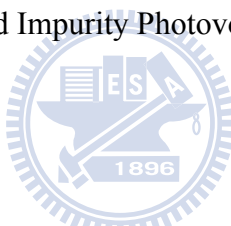
The comparison of three generations of photovoltaics is listed as below:

Table1.1 The comparison of three generation photovoltaics (Marketing)

Generation	Category	Advantage	Disadvantage	η
First <u>wafer based</u>	Single Crystalline Poly Crystalline	1. Excellent spectral response in all wavelengths 2. Low reflective alkaline textured surface 3. Precise printing and superior silver contact to assure easiness of automatic soldering and high adhesion of contact	1 .Higher use in Si wafer. 2. Limitation and bottleneck of the efficiency.	Single ~18% Poly ~16%

Generation	Category	Advantage	Disadvantage	η
Second Thin film	μ-Si	1. Stable 2. Higher efficiency than other types of a-Si 3. Manufacturing process is simpler and the cost is lower	Complicated manufacturing process Efficiency is lower than single crystalline	~8%
	a-Si	1. Low material cost. 2. Appearance in homogeneous color. 3. Can be placed on facade, window glass and even any non-flat surface.	The Efficiency and stability are worse than single- and poly crystalline silicon.	5~7%
	GaAs (III-V)	1. High efficiency 2. Usability in space 3. Stability	Hard in fabrication Costs are too high. As is toxic	> 25%
	CdTe (II-VI)	Efficiency higher than a-Si	Cd is Toxic	~11%
	1.CuInSe$_2$ 2.CIGS	1. Tunable in bandgap 2. Stability	Difficulty in process Costs are too high.	19~30%
Generation	Category	Advantage	Disadvantage	η
Third Ultra-high efficiency	1.Tandem 2.Hot carrier 3.Multi e-h pair	1. Ultra-high efficiency 2. Low cost 3. Un-toxic	Immature of technology	~10% **Lab.** Theory calculate
	DSSC	1. Colorful, 2. Low-cost 3. Large area 4. Flexible	1. Lack of long-term stability 2. Deterioration of organic dye	~4% (F) ~12% (S)
	Polymer	1. Flexible 2. Easy in fabrication	Low efficiency	~5%

1-2 Third Generation Photovoltaics

1-2.1 Efficiency Losses in Standard Cells

The two most important mechanisms for the power loss in single-junction photovoltaic cells are photon energy ($h\nu < E_g$) not been absorbed (1 in Fig.1.3 [4]) when incident energy less than the bandgap, and excess photon energy ($h\nu > E_g$) loss through lattice thermalization (2 in Fig.1.3) when incident energy is large than the bandgap. The other three losses are from junction (3 in Fig.1.3), contact voltage (4 in Fig.1.3) and recombination (5 in Fig.1.3) from conduction band to valence band.

For tackling the most important two losses in standard cells, there are few approaches: (1) Increase the number of bandgap for photon absorbing from a broad spectrum; (2) Capture carrier before they thermalize to band edge; (3) Multiple carrier pair generation per high energy photon or single carrier pair generation with multiple low energy photons.
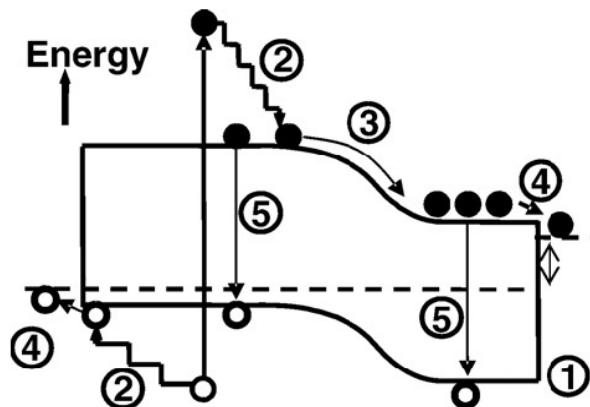

Fig.1.3. Loss processes in standard solar cells: (1) non-absorption of below band gap photons; (2) lattice thermalisation loss; (3) and (4) junction and contact voltage losses; (5) recombination loss. [4]

1-2.2 Third Generation Photovoltaics: Tandem Cells

In this section, we shall introduce more detail about the principle of Tandem Cells. In Fig.1.3, it shows that photons of a shorter wavelength probably lose their energies in a standard cell through thermalization because of the larger energy than the bandgap of the material, and photons of a longer wavelength are transparent to the material due to the lower energy than its bandgap.

With this concept, we shall improve the utilization efficiency of broadband solar photons in a photovoltaic device with a graded bandgap system: Tandem solar cells
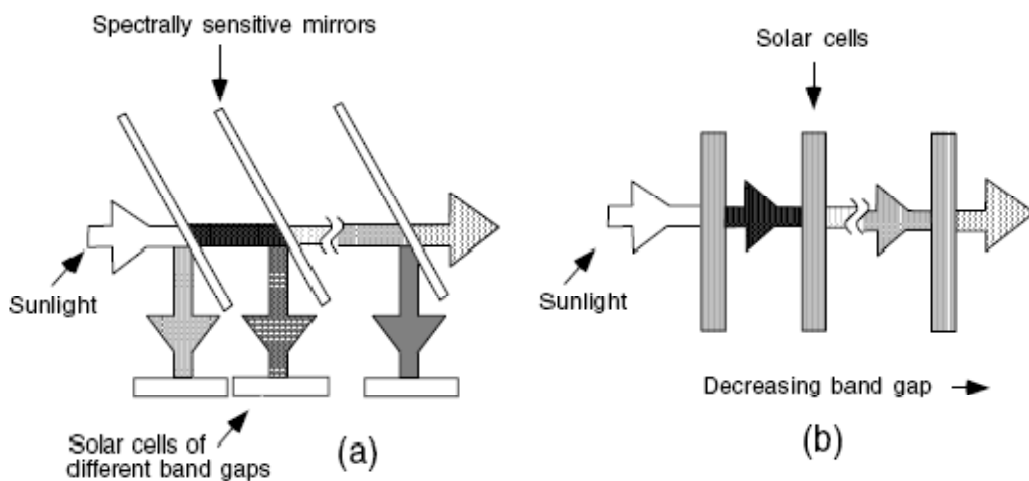

Fig.1.4 Tandem cell concepts: (a) spectrum splitting; (b) cell stacking. [5]

Due to the high entropy generation rate [5], the photon energy loses rapidly in single junction cells while photon's energy exceeds the bandgap. One approach to reduce this loss is to subdivide the broad solar spectrum into different energy ranges and to convert each range with a well-matched bandgap cell (Fig.1.4). The following Table.1.2 shows that converted efficiency under one sun and maximum conversion depends on different number of junction solar cells. [6]

Table 1.2 Efficiency depends on different stack solar cells.

Junctions in solar cell	1 sun η	Max con. η
1 junction	31.0 %	40.8 %
2 junctions	42.9 %	55.7 %
3 junctions	49.3 %	63.8 %
∞ junction	68.2 %	86.8 %

To reach > 50% efficiency, we might need more than 3-stack tandem or equivalent (assuming it can reach ~80% of a detailed balance limit). Table1.3 shows the theoretical efficiency under different numbers of stack cells.

Table 1.3 Efficiency optimal bandgap depend on different stack solar cells.

Stack number (n)	Value of bandgap(eV)	η (%)
2	1.7	42.9
3	1.5, 2	49.3
4	0.6, 1.11, 1.69, 2.48	62.0
5	0.53, 0.95, 1.4, 1.93, 2.68	65.0
6	0.47, 0.84, 1.24, 1.66, 2.18, 2.93	67.3
7	0.47, 0.82, 1.19, 1.56, 2.0, 2.5, 3.21	68.9
8	0.44, 0.78, 1.09, 1.4, 1.74, 2.14, 2.65, 3.35	70.2

1-3 Motivation and Overview of Our Thesis

The performance in single junction photovoltaics was limited to 31% when detail balance limit given by Shockley and Queisser is considered.[7] If we use the maximal artificial concentration of sunlight (46,200 suns), and make the sunlight illuminate directly on the battery, we can reduce junction and contact voltage loss, which can help efficiency increase to 40.8%.

All Si QD Tandem Cell first suggested by Green [6],[7] is a novel strategy for the first approach mentioned before to reduce loss in a standard cell. Tandem cells based on Si NCs embedded in dielectric matrices could provide a higher efficiency than the conversion of single-junction photovoltaics. In order to reduce the loss of $h\nu > E_g$, the strategy is to subdivide the broad solar emission spectrum into different parts and convert each part with a single cell of a well matched bandgap.
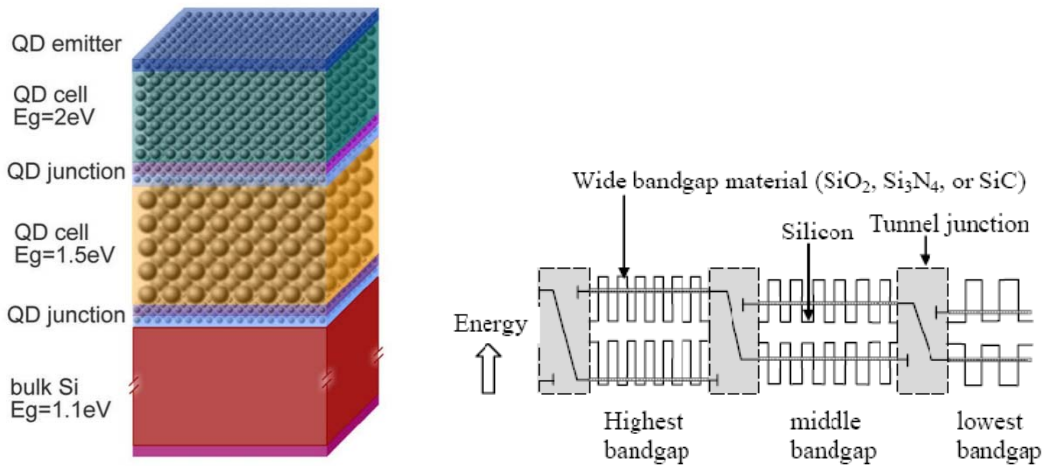

Fig.1.5 (a) Schematic of a possible design of an all silicon tandem cell based on QD superlattices. (b) The basic concept is to provide cells of different effective bandgap by varying the layer thickness in superlattices. [8]

The schematic in Fig.1.5[8] shows a possible design of the all Si-based tandem cell of the third generation photovoltaic. Si QDs are a critical feature for the all Si-based tandem cell.
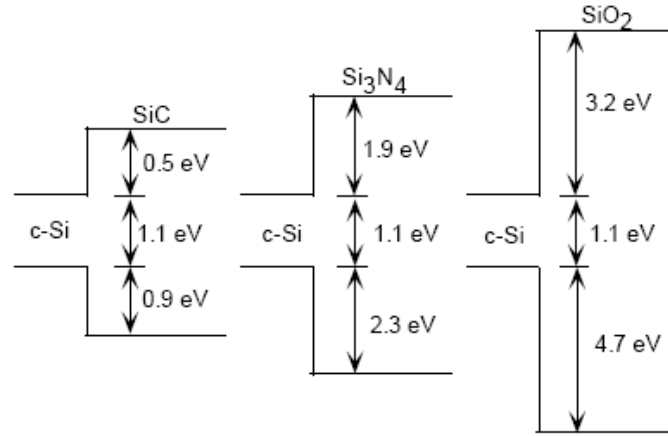

Fig.1.6 Indicative bulk band alignments between crystalline silicon and its carbide, nitride and oxide. [9]

The effective bandgaps of the two uppermost cells are controlled by their respective QD's size dispersed in higher bandgap dielectric materials, such as silicon oxide (E_g = 9eV), nitride (E_g = 5.3eV) or carbide (E_g = 2.5eV) via quantum confinement (see Fig.1.6[9]). As the absorption range on the top cell is in shorter wavelengths or the higher energy photons, we choose the larger bandgap cell uppermost, and the lower cell absorb longer wavelengths or low energy photons, each cell absorbs the light it can most efficiently convert.

The main purpose of this thesis is to investigate the structural, optical, electrical properties of Si NCs embedded in silicon dioxide matrices for third generation photovoltaic applications.

In Chapter 2, we will describe the preparation of our fabrication process including

the sample cleaning, fundamental principle of RF magnetron co-sputtering and sputtering technique of our multilayer structures, last but not least, is the introduction of formation process of Si NCs through Rapid Thermal Annealing (RTA) and furnace.

Chapter 3 first points out the main reason why we need silicon rich oxide single film. The purpose of the single film is to identify chemical composition by using Fourier transform infrared spectroscopy (FTIR) to make sure it's truly are SRO film, and shall accomplish that. Then, micro-Raman spectroscopy (micro-RS), photoluminescence (PL), transmission electron microscopy (TEM), X-ray diffraction (XRD) will reveal more experiment data and properties of Si NCs.

Chapter 4 focuses on the electrical property

Chapter 5 summaries all the data of each chapter, and discusses the improvement which we may need.
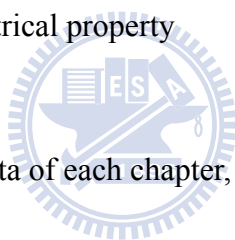
Chapter 2. Principle and Fabrication of Si NCs thin films

2-1. Quantum Confinement Effect: Si Nanocrystals (Si NCs)

From three-dimensional time-independence Schrödinger's equation (S.E.):

$$-\frac{\hbar^2}{2m}\nabla^2\psi(\vec{r})+V(\vec{r})\psi(\vec{r})=E\psi(\vec{r}) \tag{2.1}$$

we can derive E_n of a particle from an infinite potential box, the E_n will also depend on the size of this particle, and the allowed energy values are:

$$E_n=\frac{\hbar^2\pi^2}{2ma^2}n^2 \qquad n^2=(n_x^2+n_y^2+n_z^2) \tag{2.2}$$

where n_x, n_y, n_z are integers and equal to 1 for the ground state square box.

In current application, a quantum dot means particles confined in all three dimensions such as a small sphere, the **quantum confinement effect** can be observed once the size of the particle is close to wavelength of electron's wave function. When the materials are so small, their electronic and optical properties deviate substantially from those of bulk ones.
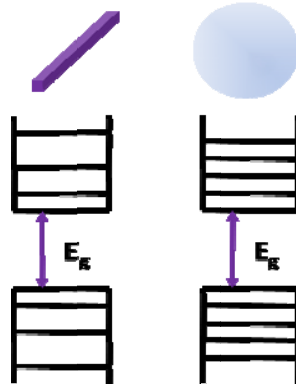

Fig.2.1 Comparison of solutions for confined energies for 1D and 3D confinement.

A particle's behaves as if it was free when the confining dimension is over excess compared to the electron's wavelength. During this density of state, bandgap remains at its original energy due to continuous energy state. However, as the confining dimension decreases and reaches a certain limit, typically in **nanoscale**, the energy spectrum turns to discrete (Fig.2.1). Hence, allowed states in a three dimensional confinement were increase as the square of the quantum number, n and there is a large energy gap between the first and higher energy states

A high density of discrete VB states results (see Fig.2.2). Interactions between the 5 degenerate conduction band valleys also splits the degeneracies associated with the CB [10]. Proximity to other dots causes additional splitting of allowed states causing each level in Fig.2.2 to broaden into a band of width determined by the dot spacing. Variations in the dot diameter between dots will cause additional overlapping of the energies of allowed and non-allowed states.
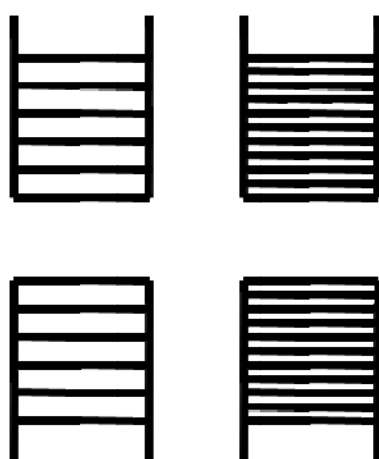

Fig.2.2 Effect of silicon's anisotropic CB mass (left) and dot size increase of 10% (right) on available energy states.

As a result, bandgap becomes tunable or size dependent. This ultimately results a

blue shift in optical illumination as the size of the particles decreases to nanoscale. In

Fig. 2.3 shows the normalized PL spectra of the SiO_x/SiO_2 films [11]. A strong

blueshift from 960 to 810 nm with decreasing nanocrystals size was observed.
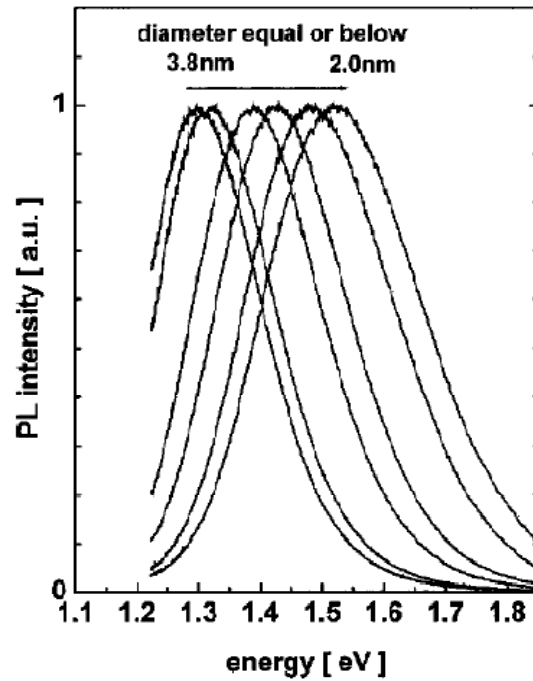

Fig.2.3 Normalized photoluminescence spectra showing a blue shift correlated with

the crystal size. [11]

2-2 RF Magnetron Co-Sputtering and Multilayer Fabrication

2-2.1 Pre-Procedure of Our Substrates

In the beginning, we divide our test sample into two groups, part of one is Si substrates including p-type and n-type, those samples are normally use for photoluminescence (PL) analyze, Fourier Transform Infrared Spectroscopy (FTIR), electrical property measurement, X-ray diffraction (XRD) and transmission electron microscopy (TEM). In order to avoid Si signal of single crystal at 520 cm^{-1} in micro-Raman spectrum, we choose quartz as substrate to deposit the same structure.

Before the Si substrates were loaded into sputtering chamber, they were cleaned by doing the standard preliminary RCA process. (see Table.2.1)

Table 2.1 Clean process of Si substrate.

Preliminary RCA clean	
Step 1	5 min in DI water rinse
Step 2	10~15 min in (3 : 1) proportion H_2SO_4 / H_2O_2
Step 3	5 min in DI water rinse
Step 4	10~15 sec in (1 : 100) proportion HF/ H_2O
Step 5	5 min in DI water rinse

In the cleaning process of quartz, we use the sonic approach to get rid of the organic contaminates on quartz substrate.

2-2.2 Operation Principle of RF Magnetron Co-Sputtering

The basic principle of sputtering is to accelerate the ion to bombard the solid surface, after ion and atomic in solid surface exchange the momentum, atoms will spill from the solid surface, this phenomenon called **sputtering**. Sputtering is a vacuum coating method. Usually, the cathode is the target, while the anode (anode) is the sample.

Sputtering mainly depend on the state of the plasma ions and free radicals. Plasma is also known as the fourth state of matter. Plasma's creation is similar to phase changes in matter. By applying energy (such as high heat) to matter, a solid melts to become a liquid, and a liquid evaporates to become a gas. By adding enough energy (such as RF or microwave), a gas can be broken down into plasma.
In this state the plasma contains charged atoms, particles, ions and free radicals. Plasma is very chemically reactive due to its high energy state, making it very useful for changing the properties of material.

To ignite the plasma of the sputtering gas, cathode should be added to hundreds of volts. The voltage added on cathode relative to the anode is negative, it shows when Ar atoms become Ar ions, and they will be accelerated and impacted target, after collision, the atoms on the target surface flight and deposit on the substrate, that's the principle of sputtering (Fig.2.4).
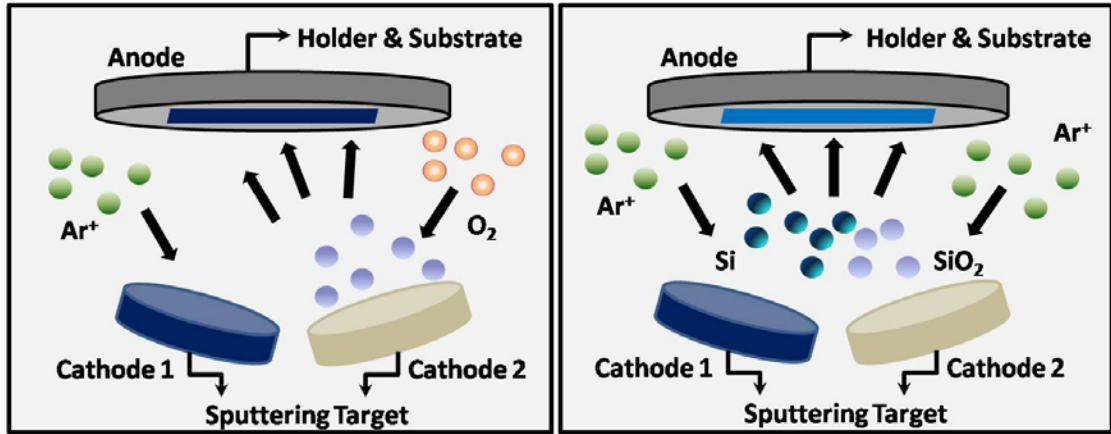
Fig.2.4 Operation of magnetron sputtering and co-sputtering.

2-2.3 Multilayer (SRO/SiO$_2$) Structure Fabrication

In order to achieve silicon rich oxide (SRO) or SiO$_x$ composition, Si and SiO$_2$ sputtering target were used. By adjusting thickness of our film, we will control the time of switch of shutter.

We also adjust the power of Si and SiO$_2$ target to control the chemical composition proportion of Si and SiO$_2$ to achieve a non-stoichiometry SiO$_x$ (x < 2) film. For a multilayer structure, the SRO films need two power opened at the same moment and SiO$_2$ films need power opened only on target SiO$_2$.

Fig.2.5 shows the as-deposited multilayer structure of this thesis. For different purpose, we choose the total SRO thickness the same but different pair number to understand the properties on micro-Raman and PL spectrum. We also control the total multilayer thickness the same to figure the electrical characteristic out (see Fig.2.6).

Fig.2.5 As-deposited SRO/ SiO$_2$ multilayer with each SRO single film in different

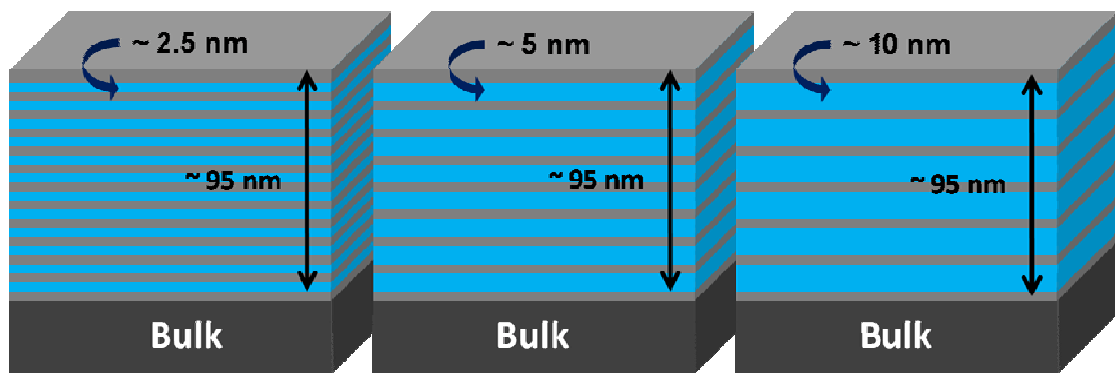thickness but total thickness of SRO films are the same.

Fig.2.6 As-deposited SRO/ SiO$_2$ multilayer with each SRO single film in different

thickness but total thickness of SRO/ SiO$_2$ multilayer are the same.

2-3 Formation of Si NCs

2-3.1 Thermal Annealing Process: Rapid Thermal Anneal (RTA) and Furnace

The main difference between the two thermal processes is furnace can be used in multi-wafer batch, while the RTA is a monolithic (single wafer) process. However, furnace process conventionally needs longer time, ten few minutes even hours, but RTA process will be achieved at few seconds.

In traditional case, the Si NCs precipitation in SRO film during sustain in high temperature annealing (1000°C or 1100°C) about 1~2 hours or undergo the RTA at 900°C to form Si NCs.
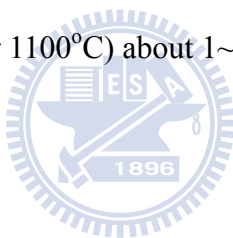
In the TEM images (Fig.2.7), we can see that the crystallinity after furnace 1100°C 1 hour (Fig.2.7 (a)) is probably better than RTA 1050°c 30 sec (Fig.2.7 (b)), that might due to the longer annealing time in furnace than RTA process. In this thesis, we also try another thermal annealing process, the furnace process followed by RTA process(R+F). First of all, we let our multilayer structure in RTA 1050°C 30 sec, after that, furnace 1100°C 1 hour with N_2 atmosphere at 50 sccm will be continued.
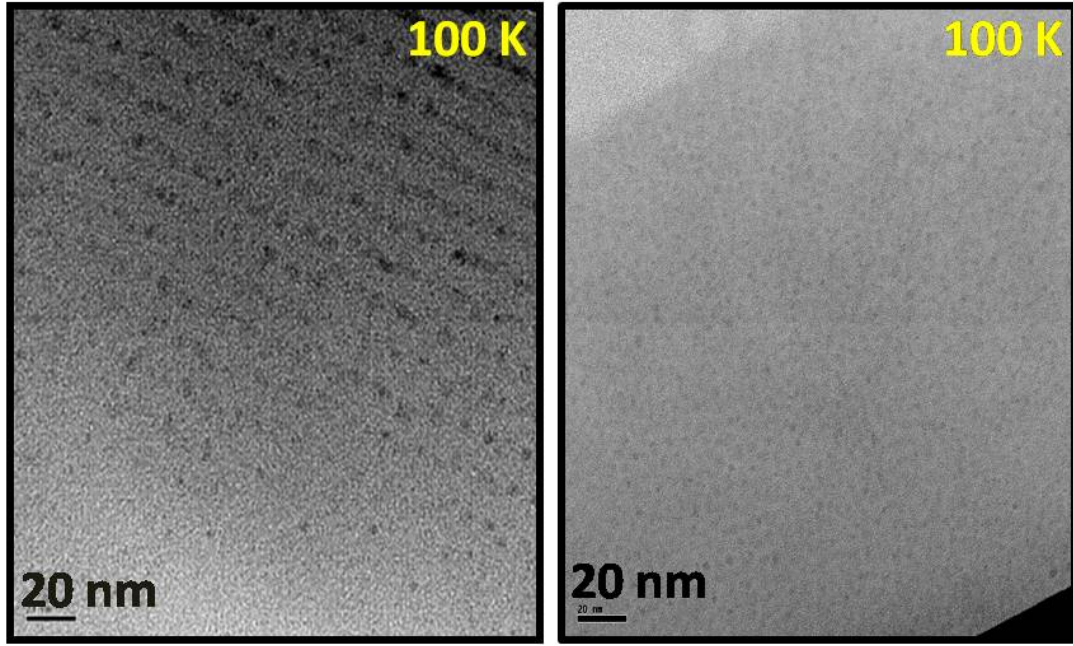
Fig.2.7 (a) TEM image of Si NCs after furnace 1100°C 1 hour;

(b) TEM image of Si NCs after RTA 1050°C 30s.

In this thesis we use three different conditions on thermal process, the detail were

showed as table2.4:

Table 2.2 Three thermal annealing conditions in this thesis.

Condition Number	Thermal annealing process
Condition1	RTA 1050 ^{o}C 30s
Condition2	RTA 1050 ^{o}C 30s + Furnace 1100 ^{o}C 1 hour
Condition3	Furnace 1100 ^{o}C 1 hour

2-3.2 Formation of Si NCs: Phase Separation of SRO Film

In case of SiO_x (x < 2), the bonding configuration and the SiO_x composition corresponding to the several (Si-O_{4-y}-Si_y, $0 \leq y \leq 4$) [12] bonding tetrahedral to which the Si next neighbors of the vibrating O-atom may belong. In Fig.2.8, the excess Si in SRO film will precipitate during high temperature annealing process due to phase separation of Si and SiO_2.
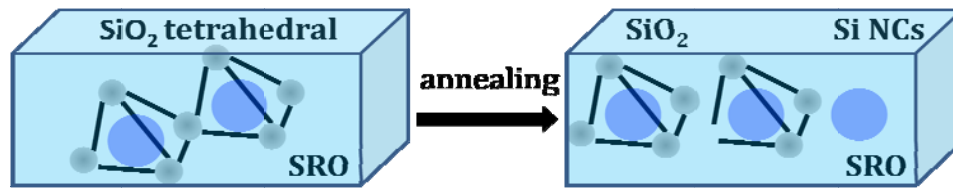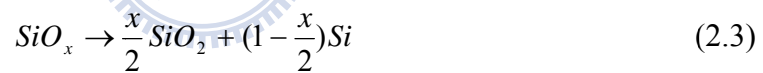

Fig.2.8 Phase separation after thermal annealing.

There are some research suggested that this phase separation occurs according to the following:

$$SiO_x \rightarrow \frac{x}{2} SiO_2 + (1 - \frac{x}{2})Si \qquad (2.3)$$

From Eq. (2.3), we realize that the density of the QDs might be more or less varied by the composition of the SRO films. We also know that the nucleation of the QDs after thermal process will tend to fall if we increasing oxygen content.
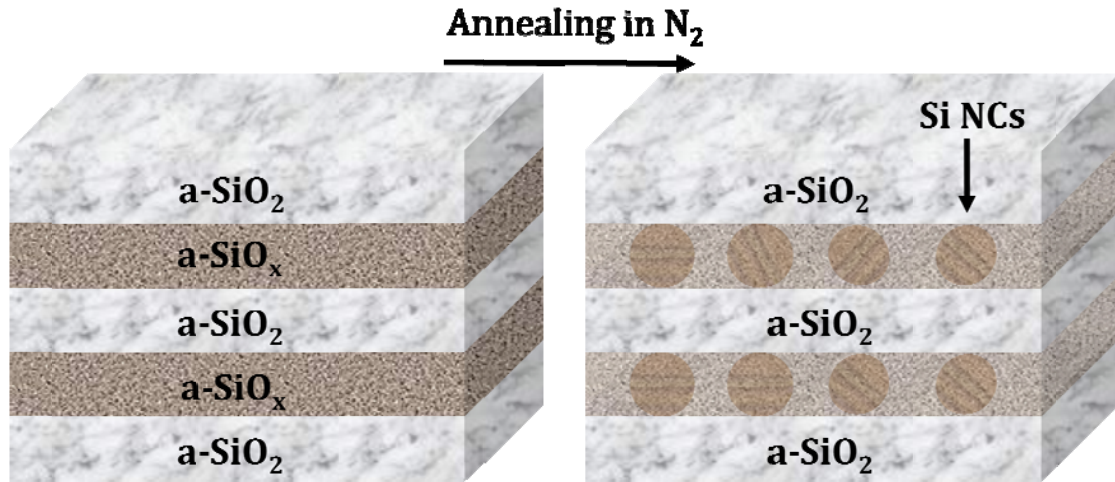
Annealing in N$_2$

Fig.2.9 Schematic of as-deposited a-SiO$_x$/SiO$_2$ multilayer structure and nucleation

after annealing in N$_2$.

Si NCs formation in SRO films after thermal process is shown in Fig.2.9, in this thesis, based on Eq. (2-3), the density of Si NCs depend on the Si proportion of the SRO films, that's why we vary the sputtering power on Si target. The higher power we use on Si target the higher percentage of Si content we have in SRO film. In addition, to investigate quantum confinement effect, we also change the thickness of the SRO film.

Chapter 3. Characterization of Si NCs thin films

3-1. Introduction

To understand the quantum confinement effect of our Si NCs embedded in SiO_2 matrix structure, we may need more information from micro-Raman spectra, PL spectra and TEM, those above-mentioned instruments shall work on the SRO/SiO_2 multilayer later to check the signal exactly from Si NCs.

After thermal annealing, we want to know if the formation of Si NCs exists or not. By using micro-Raman spectra we realize the volume fraction of crystalline of Si NCs; by using PL spectra we understand the optical gap of oxygen vacancy, Si=O double bond, interface state between Si NCs and SiO_2 matrix, impurity state and quantum confinement effect of Si NCs. We also identify the phase separation of SRO/SiO_2 multilayer by using Fourier Transform Infrared Spectroscopy (FTIR). TEM shows the magnify images from internal structure of SRO/SiO_2 multilayer. Table3.1 lists the main function of each instrument we used in this thesis.

Table 3.1 The major functions of instrument in this thesis.

FTIR	Analysis of structure and composition of SRO single layer
micro-Raman	Detect the fraction of crystalline of Si NCs
PL	1. Band gap determination 2. Impurity levels and defect detection 3. Recombination Mechanisms
TEM	Observation of the magnify image from internal structure of objects

3-2 Analysis of SRO single layer by Fourier Transform Infrared Spectroscopy (FTIR)

3-2.1 Fundamental of Infrared Absorption Spectroscopy

Basic theory

FT-IR stands for **F**ourier **T**ransform **I**nfra**R**ed, the preferred method of infrared spectroscopy. In infrared spectroscopy, IR radiation is passed through a sample. Some of the infrared radiation is absorbed by the sample and some of it is passed through (transmitted). The resulting spectrum represents the molecular absorption and transmission, creating a molecular fingerprint of the sample. Like a fingerprint no two unique molecular structures produce the same infrared spectrum. This makes infrared spectroscopy useful for several types of analysis.

The normal instrumental process is as follows:

1. The Source: Infrared energy is emitted from a glowing black-body source. This beam passes through an aperture which controls the amount of energy presented to the sample (and, ultimately, to the detector).

2. The Interferometer: The beam enters the interferometer where the "spectral encoding" takes place. The resulting interferogram signal then exits the interferometer.

3. The Sample: The beam enters the sample compartment where it is transmitted through or reflected off of the surface of the sample, depending on the type of analysis being accomplished. This is where specific frequencies of energy, which are uniquely

characteristic of the sample, are absorbed.

4. The Detector: The beam finally passes to the detector for final measurement. The detectors used are specially designed to measure the special interferogram signal.

5. The Computer: The measured signal is digitized and sent to the computer where the Fourier transformation takes place. The final infrared spectrum is then presented to the user for interpretation and any further manipulation.

Instrument

The samples of SRO single film were analyzed by Fourier Transform InfraRed on ASTeX PDS-17 System (see Fig.3.1), and the IR absorbance of the films was measured in the spectral range from 720 cm^{-1} to 1350 cm^{-1} with a resolution of 1 cm^{-1}. Dry nitrogen purges within the instrument were used to avoid residual water-vapor absorption in the region between 1200 and 1800 cm^{-1}.

Fig.3.1 Fourier Transform InfraRed Spectroscopy (ASTeX PDS-17 System)

Phase separation in SRO film on IR absorption spectrum

In this section, Fourier transform infrared spectroscopy (FTIR) was used in the study of the IR absorption spectrum of SRO film. The structure of SRO is often represented as a mixture of $Si\text{-}O_{4-y}\text{-}Si_y$, ($0 \leqq y \leqq 4$) complexes, as previously

mentioned. Before we discuss the results of FTIR measurement in SiO_x film, the main features of FTIR in SiO_2 are listed as Table 3.2 and fig.3.2:

Table 3.2 Vibrational properties of silicon dioxide.

Symbol	Vibrational mode	Wavenumber(cm^{-1})
T_1O	Si-O Rocking mode	460~465 cm^{-1}
T_2O	Si-O Bending mode	800~805 cm^{-1}
T_3O	Asymmetric Si-O-Si stretch mode with adjacent O atom in phase (TO mode)	1045~1090 cm^{-1}
T_4O	Asymmetric Si-O-Si stretch mode with adjacent O atom out of phase (LO mode)	1150~1200 cm^{-1}
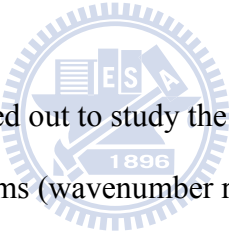
Fig.3.2 The comparison of absorption spectra of a-SiO_2 films with using reactive co-sputtering target and single silica target. [**13**]

27

As Fig.3.2 [13] show, the T_3O mode reveals the strongest absorbance, due to Si-O-Si stretching transverse optical (TO) mode, in this section, the attention is focused on the stretching peak of Si-O-Si structural entity, around 1000~1090 cm^{-1}. In as-deposited SiO$_x$ film, the T_3O peak located in the range from 978.72 cm^{-1} to 1040 cm^{-1}[12], increase linearly according to the following formula:

$$\nu(cm^{-1}) = 978.72 + 30.63 \cdot x \qquad (3.1)$$

which depend on the x content of SiO$_x$. After annealing, the peak of the T_3O mode will shift, this process come from the phase separation of our SiO$_x$ film.

3-2.2 Experimental Results and Discussions

FTIR measurements were carried out to study the bonding configuration and SiO$_x$ composition of the SRO single films (wavenumber range of 720-1350 cm^{-1}, with a step size of 1 cm^{-1}). In this work, the studied samples were silicon rich oxide single film with power 110W and 50W for Si and SiO$_2$ target co-sputtering respectively. The thickness of SRO film is 284 nm approximately. The sample thicknesses were determined by α-step measurement. The thermal annealing process on the SRO single films were carried out at 1100° C for 1 hours and 1050°C 30 s individually.

J.U. Schmidt mention the up-shift of IR absorbance peak of as-deposited SRO film to higher wavenumber from 1041 cm^{-1} to a final position of about 1052 cm^{-1},1063 cm^{-1}, 1072 cm^{-1} when SRO samples were during RTA 30s at 850°C, 950°C and 1050°C. This behavior suggests that phase separation appears in SiO$_x$ layers of the multilayers after annealing (see Fig. 3.3[12]).
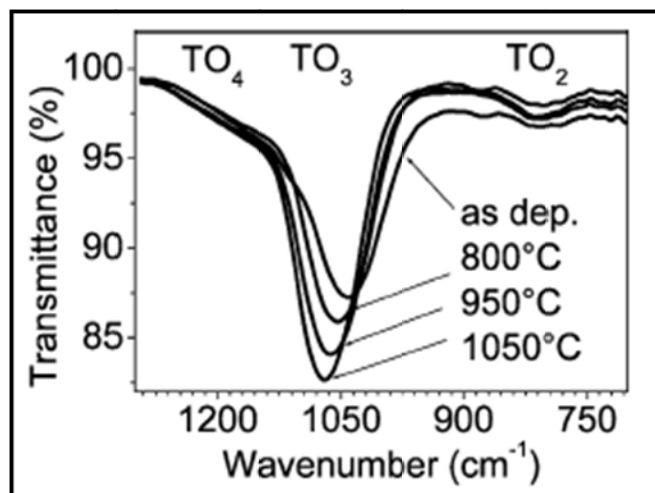
Fig.3.3 IR spectra of SRO single film (53.8nm) sample before and after RTA. [12]

Fig. 3.4, 3.5 and fig.3.6 show the FTIR spectra of SRO single film in the as-deposited, RTA $1050^{o}C$ 30s and $1100^{o}C$ 1 hour, respectively, in the wavenumber range of 720 cm^{-1} to 1340 cm^{-1}. Table 3.3 summarizes the peak position, intensity and FWHM of the three different processes.
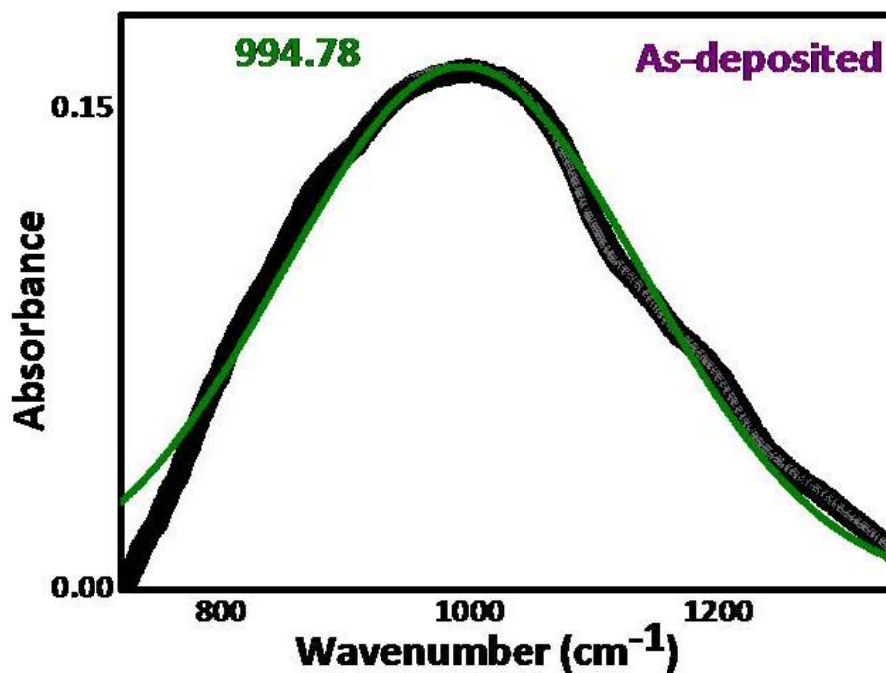

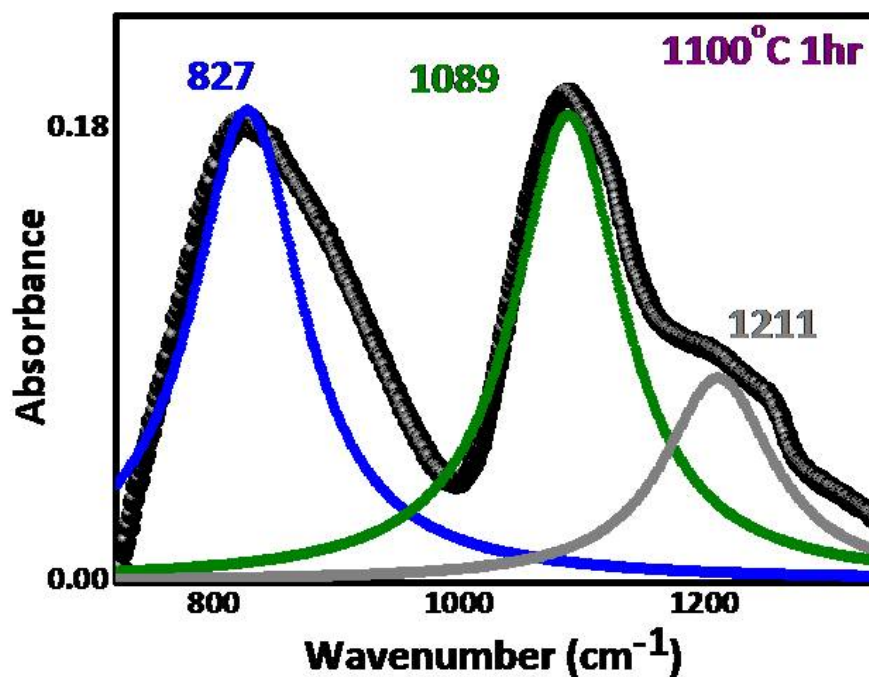**Fig.3.4** FTIR spectra of the SRO single film at the as-deposited.

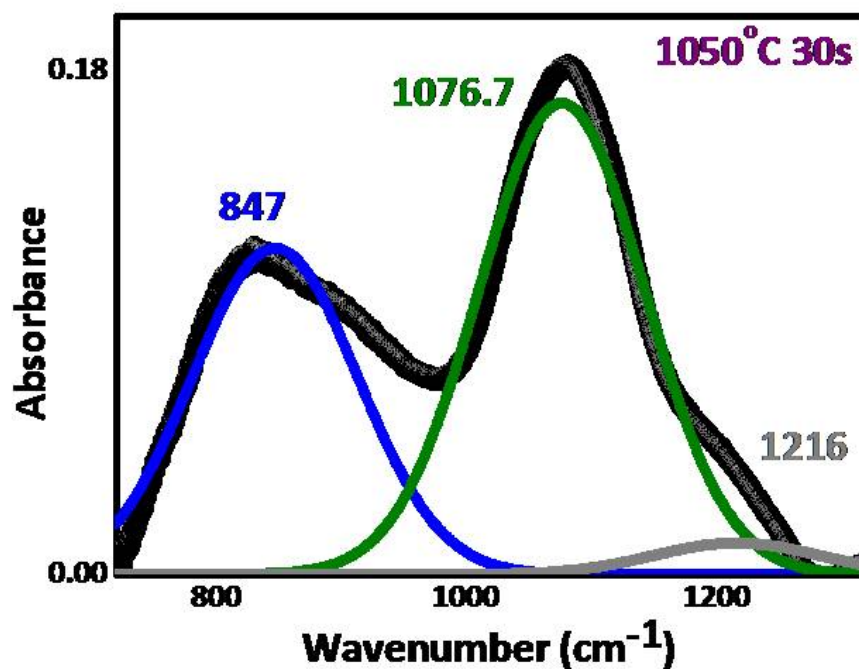**Fig.3.5** FTIR spectra of the SRO single film at the 1100°C 1 hour.

Fig.3.6 FTIR spectra of the SRO single film at the 1050°C 30s.

30

Table 3.3 Lists of the maximum absorbance, peak position, and full width at haft maximum (FWHM) of the TO mode peak of the SRO single film samples.

	As-deposited	1050$^{\text{o}}$C 30s	1100$^{\text{o}}$C 1hr
Peak position (cm^{-1})	994.78	1076	1089
Intensity (a.u)	0.1616	0.1684	0.1849
FWHM (cm^{-1})	345.39	115.08	107.34
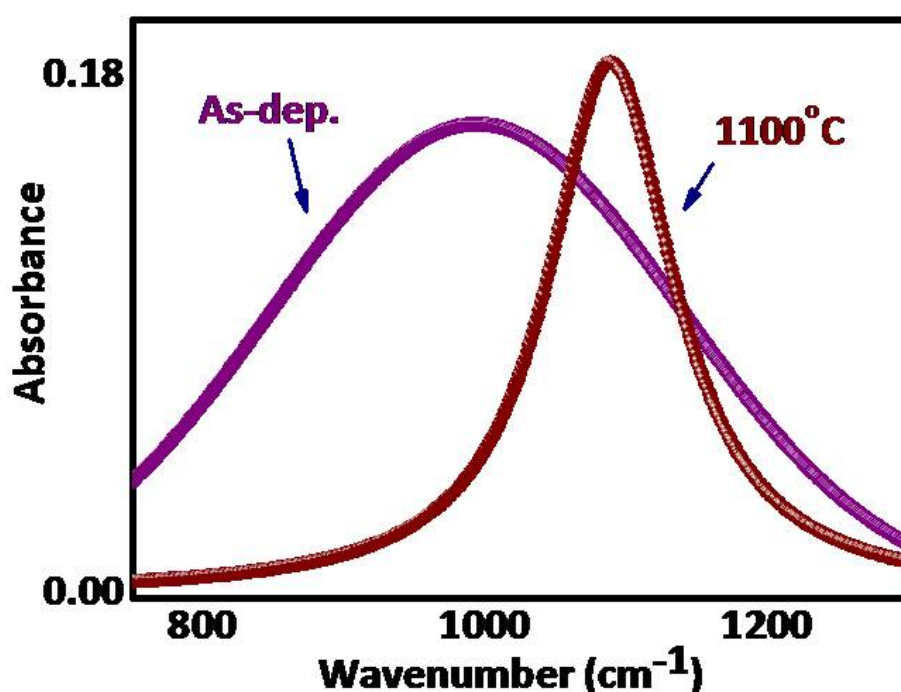
Fig 3.7 The peak shift of FTIR after thermal annealing.

From table3.3, the peak position shift when we anneal our sample in 1100$^{\text{o}}$C 1 hour and RTA 1050$^{\text{o}}$C 30s, it shift from 994.78 cm^{-1} to 1076 cm^{-1} and 1089 cm^{-1}, this result was matched with the previous work from J.U. Schmidt. Furthermore, the increase of the FWHM may due to the ordering in the oxide layer is inhomogeneous through the layer thickness.[14]

3-3 Analysis of Multilayer (SRO/SiO₂) by Micro-Raman Spectroscopy

3-3.1 Fundamental of Micro-Raman Spectroscopy

Basic theory

Micro-Raman spectroscopy has been known as a powerful characterization technique for various semiconductor and insulator materials. It can help us to detect local atomic arrangements through bond frequencies and the lattice-vibration (phonon) frequencies of the Si-Si bond. Fig.3.8 schematically shows the principle of laser scattering [15]. Raman spectroscopy is based on the Raman effect, which is the inelastic scattering of photons by molecules. It was initially reported by Raman in 1928 [16].
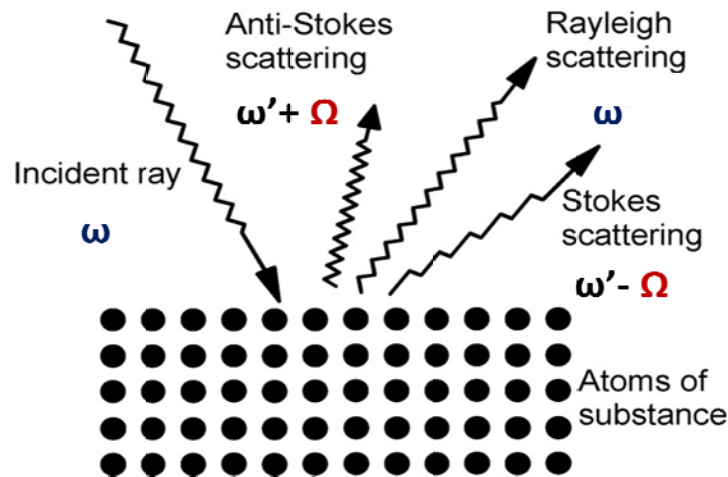

Fig.3.8 Schematic model of laser scattering. [15]

Scattering occurs when a beam of monochromatic light passes through a crystal, if the frequency (wavelength) of the scattered radiation is analyzed, not only is the

incident radiation wavelength observed via elastic scattering (**Rayleigh scattering**), but also a relatively small amount of radiation is scattered inelastically at some different wavelengths, referred to as **Stokes** and **anti-Stokes** Raman scattering (see Fig.3.9), in most of case, we prefer to focus on **Stoke** side due to the larger intense.
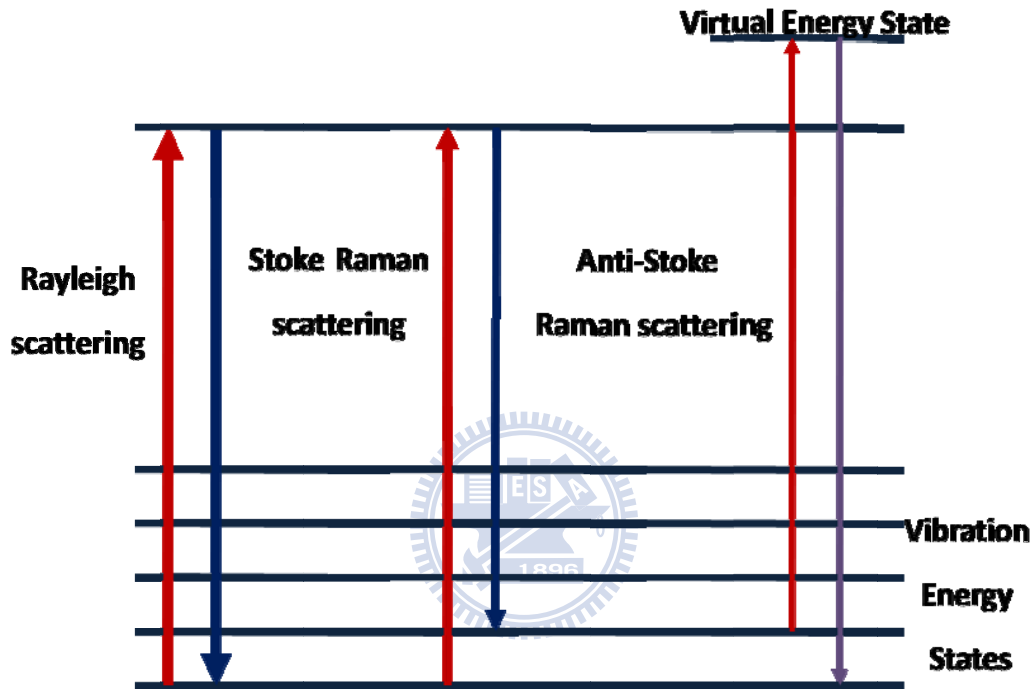

Fig.3.9 Energy level diagram showing the states involved in Raman signal.
The line thickness is roughly proportional to the signal strength from the different transitions.

Fig.3.10 shows a photon was inelastic scattered in crystal, and accompanied by the creation or annihilation of a phonon. Conservation of energy and momentum are mathematically present as wavevector selection rule:

$$\hbar\omega + \hbar\Omega = \hbar\omega'$$

(3.1)

where $\hbar\omega$ is the energy of photon, $\hbar\Omega$ is the energy of the phonon, $\hbar\omega'$ is the energy of the scattered photon.
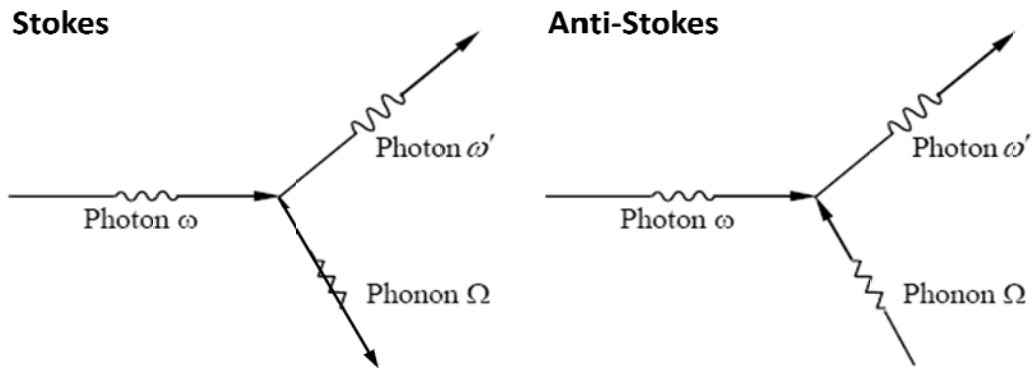
Fig.3.10 Raman scattering including release (**Stoke**) and absorption (**Anti-Stoke**) of a phonon.

Instrument

In this thesis, samples were analyzed by micro-Raman measurement on High Resolution Confocal Raman Microscope (Lab RAM HR Raman Microscope), we use both laser on He-Ne 632.8 nm wavelength and laser on diode pumped solid state (DPSS) 488 nm wavelength. (see Fig.3.11)
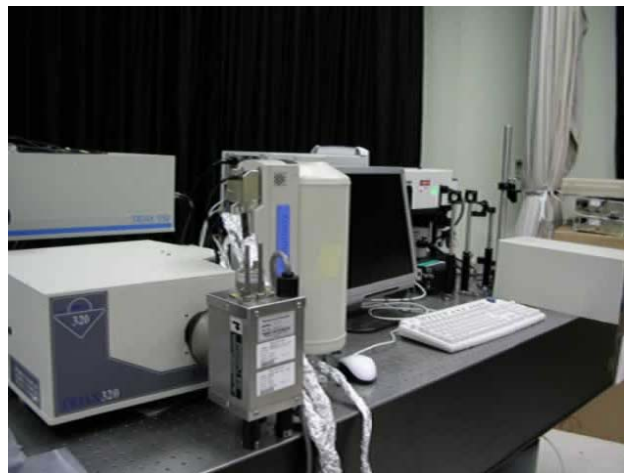

Fig.3.11 High Resolution Confocal Raman Microscope

The illuminated spot size was about 10μm in diameter, and the power of the laser after multi-filtering was 15mW. Before measuring of the Raman spectra, p-type Si substrate was used to calibrate the crystalline signal on **520 cm^{-1}**.

Volume fraction of crystallinity

Micro-Raman spectra can detect the presence of crystallization of Si NCs. For bulk crystalline silicon (c-Si), the triple degenerate optical phonons display in the first-order Raman spectrum a sharp peak at the Raman shift of **520 cm^{-1}**, and for amorphous silicon (a-Si), the first order Raman spectrum reflects the phonon density of states and presents an optical band peak at **470 cm^{-1}** [17].

Fig.3.12 shows the typical Raman spectra of two samples [18]. The curve denoted by ρ'=0.19 has been resolved into two parts: I_a, shaded; and I_c.
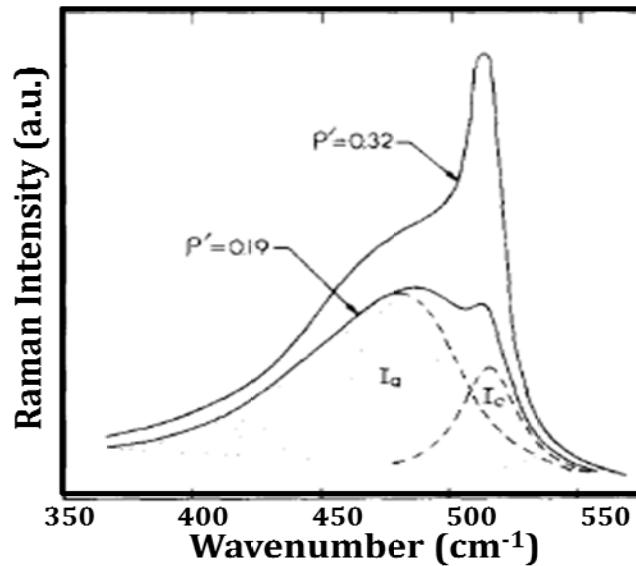

Fig.3.12 Raman intensity vs. Raman frequency for a two-phase system, microcrystallites embedded in an amorphous matrix. [18]

A typical amorphous silicon spectrum has a maximum peak position located at about **470-480 cm^{-1}**. After subtracting I_a from the total measured scattering, the remaining area under the curve is attributed to I_c, the contribution from the critical fraction of crystallinity, ρ is defined as:

$$\rho' = \frac{I_c}{I_c + I_a} \tag{3.2}$$

in which $I_c = \Sigma_c \rho_c$, $I_a = \Sigma_a (1 - \rho_c)$, where Σ is the integrated backscattering cross section over the measured frequency range. Solving Eq. (3.2) for the volume fraction of crystallinity, ρ_c, we obtained

$$\rho_c = \frac{\rho'}{\rho' + y(1 - \rho')} \tag{3.3}$$

in Eq.3.3, the meaning of y define as $y = \dfrac{\Sigma_c}{\Sigma_a}$ [18],it is the ratio of the integrated Raman cross section for c-Si to a-Si.

Full width at half maximum (FWHM)

To understand more detail about Raman spectra, we also estimate the Full width at half maximum (FWHM), in previous work from other authors, they have emphasized the FWHM on the size dependence of Si NCs, and the relation between FWHM and Raman shift.

S. Huang suggest that the FWHM value (6.7, 5.4, 4.5 cm^{-1}) are corresponding to the size of Si NCs (5.3, 7.5, and 9.8 nm) through different annealing temperature (700 ^{o}C, 850 ^{o}C, 1100°C) due to phonon confinement effects (see Fig. 3.13). For nc-Si, the

band-shape modification of the Raman peak has been explained using different theoretical models that quantify the phonon confinement. These models have become very popular because they allow the Si crystallite size to be determined [19].
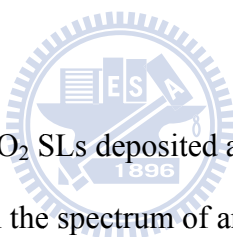
Fig. 3.13 Raman spectra for Si/SiO$_2$ SLs deposited at room temperature is a Si-like. The crystalline Si peaks in the spectrum of annealed films (dots) are fitted using a phonon confinement model considering spherical NCs (solid lines). Calculated L and annealing temperatures are indicated near the theoretical curves. [19]

In G. Faraci's work, they compare with other theoretical models of Richter et al. (RWL, [20]) and the Bond Polarization Model (BPM, [21]), these models take into account the quantum confinement effects due to the very small size of the quantum dots. Those models are roughly matched with G. Faraci's work. From Fig.3.14 we observe a quasi linear increase of the linewidth as the shift increases was mentioned by G. Faraci [22].

Fig.3.14 Full Width at half maximum of the Raman peaks against the corresponding

Raman shift. The trend is quasi-linear. [22]

From above mentioned, we might summarize that FWHM of Raman spectra

increase as the peak shift increase and size decrease.

3-3.2 Experimental Results and Discussions

Annealing condition dependence of Raman spectra in Si NCs

In this section, we will investigate the crystallization of Si NCs in SRO/SiO2

multilayer by using Raman spectra from 450 cm^{-1} to 550 cm^{-1}. Fig. 3.15 shows the

Raman spectra of as-deposited sample compared with samples under three different thermal annealing conditions (see table2.4). As-deposited sample (Black line) shows no peak in Raman spectrum; condition 1 (RTA 1050oC 30s) shows a broad peak in Raman and maximum peak position was located in **507.7 cm^{-1}**; condition 2 (RTA 1050°C 30s+Furnace 1100°C 1hr) has a more sharper peak in **515 cm^{-1}** while condition 3 has a broad peak around **518.3 cm^{-1}**.
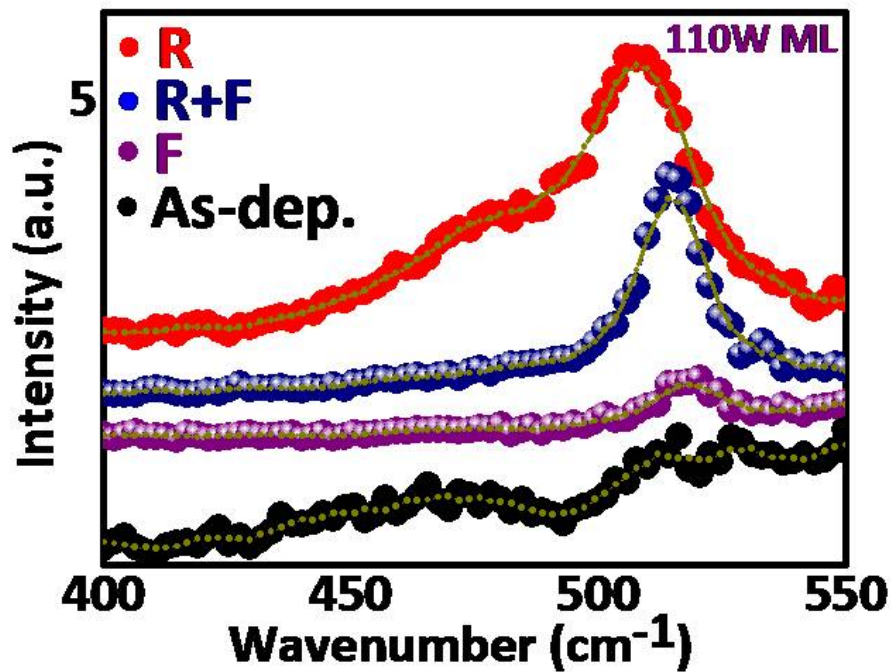

Fig.3.15 Raman spectra of a 24 pairs 5nm SRO/5nm SiO$_2$ as-deposited multilayer compared with three different thermal annealing conditions.

To realize more detail about the Raman spectra, Table 3.4 lists the peak position, FWHM, peak intensity and cross section of component of Si NCs, surface mode and amorphous silicon. The peak position of condition 1 is located at 478.7 cm^{-1} and 507.8 cm^{-1}; this means the structure from SRO/SiO$_2$ multilayer is amorphous and

poly-crystalline dominated (see Table 3.5). From Table 3.4, the peak intensity of 478.7 cm^{-1} and 507.8 cm^{-1} are 0.74 and 2.69 (a.u.) respectively, the intensity of poly crystalline are about 3.6 times of the intensity of amorphous, the detailed curve fitting are shown as Fig.3.16. The result shows us the volume fraction of crystalline of condition 1is about **51%** by solving the Eq.3.2 and Eq.3.3.

Table 3.4 List of Raman spectra depend on different thermal annealing process

	Ω_{nc} (cm^{-1})	Ω_a (cm^{-1})	Ω_s (cm^{-1})	FWHM (nc)	FWHM (s & a)	I_{nc}	I_a	I_s
Condition1	507.8	478.7	×	22.91	23.97	2.69	0.74	×
Condition2	515	×	493.1	15.02	16.13	1.82	×	0.15
Condition3	518.3	×	500.7	14.40	6.72	0.39	×	0.03

Table 3.5 Relationship between the crystallization and location of Raman spectra.

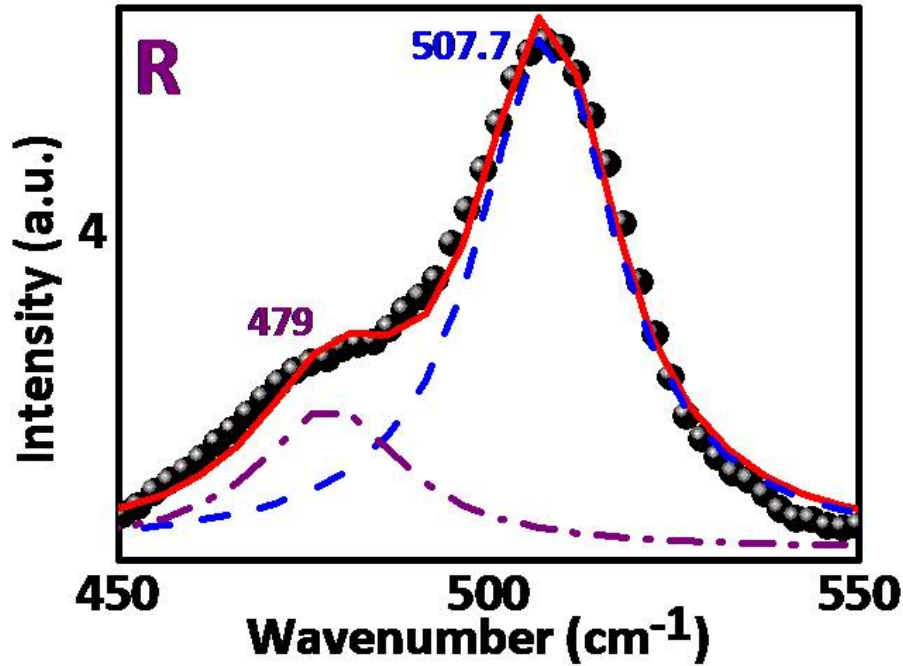|	
470 ~ 480 cm^{-1}	Amorphous
492 ~ 498 cm^{-1}	Near-surface region
500 ~ 510 cm^{-1}	Poly (Amorphous & Crystalline)
510 ~ 519 cm^{-1}	Crystalline (Depend on size)
520 ~521 cm^{-1}	Single crystal

Fig.3.16 Measured and decomposed Raman spectra of condition 1.

After RTA 1050°C 30s +Furnace 1100°C (condition 2) process, the Raman spectra was decomposed (see Fig.3.17). It clearly shows that original curve has two components including a broaden one located in 493.12 cm^{-1} (attributed to near surface region of Si NCs, see table 3.4), the other sharp one located in 515.03 cm^{-1} (attributed to the Si NCs). From Table 3.4, we see that the signal of Si NCs is 12 times the intensity of the near surface mode, which means, the critical volume fraction of crystalline of SRO/SiO$_2$ multilayer in this thermal annealing condition seems better than condition 1. It seems has the best critical volume fraction of crystalline when SRO/SiO$_2$ under condition 3 thermal annealing process due to the peak position shift to 518.7cm^{-1}, which is very close to the single crystalline (see Fig.3.18). The signal of Si NCs is 13 times the intensity of the near surface mode, even larger than condition 2 process.
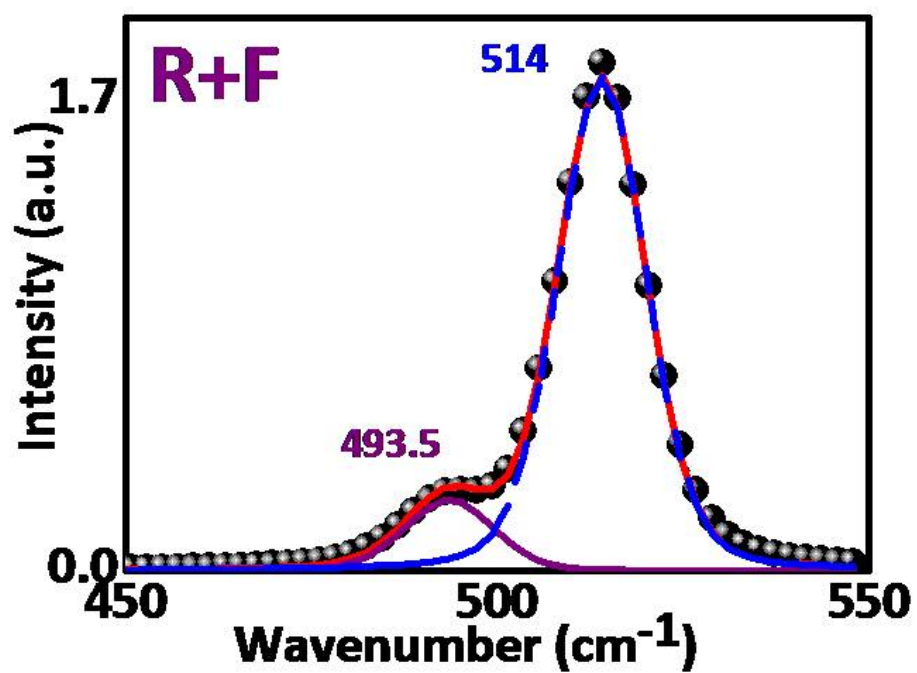
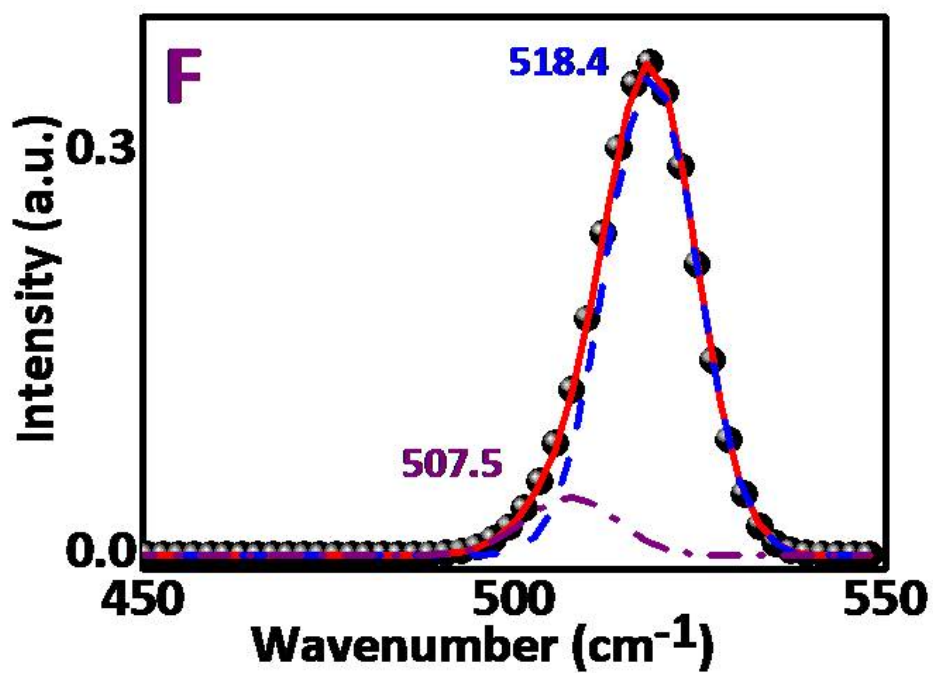**Fig.3.17** Measured and decomposed Raman spectra of condition 2.

Fig.3.18 Measured and decomposed Raman spectra of condition 3.

From Fig.3.14 and Table 3.4, the relation between FWHM and Raman shift was shown as Table3.6 and Fig.3.19. Under different thermal annealing processes, we might say that the trend is roughly closed to Fig.3.14. More detail will be discussed in following section.

Table 3.6 Relationship between the crystallization and location of Raman spectra.

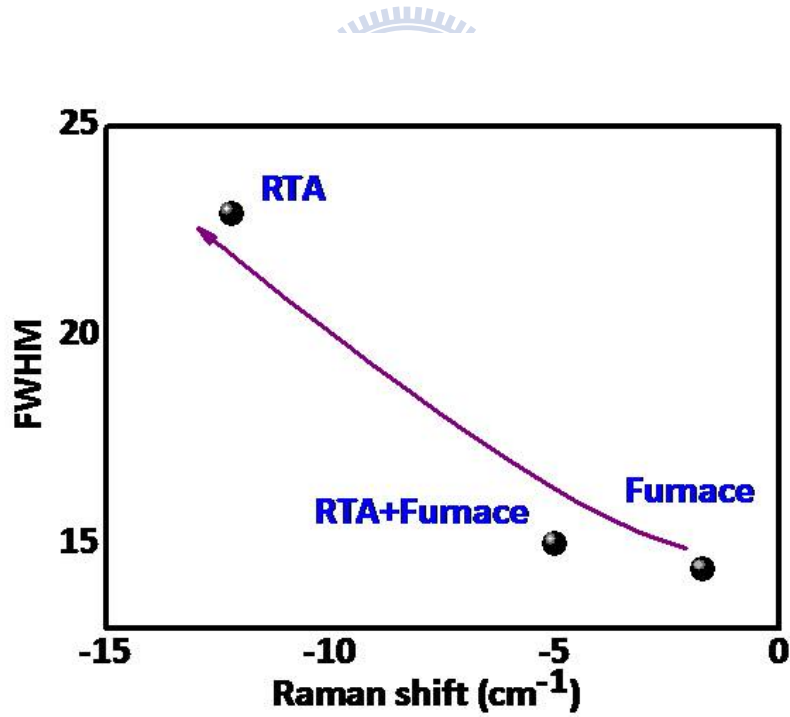| Condition	Ω_{nc} (cm^{-1})	FWHM (nc)
RTA	507.8	22.91
RTA + Furnace	515	15.02
Furnace	518.3	14.40

Fig.3.19 Relation between FWHM and Raman shift under different thermal annealing processes.

3-4 Analysis of Multilayer by PL Spectroscopy

3-4.1 Fundamental of PL Spectroscopy

   Photoluminescence (**PL**) spectroscopy is a contactless, nondestructive method of probing the electronic structure of materials. Light is directed onto a sample, where it is absorbed and imparts excess energy into the material in a process called photo-excitation (see Fig.3.20). One way this excess energy can be dissipated by the sample is through the emission of light, or luminescence. In the case of photo-excitation, this luminescence is called photoluminescence. The intensity and spectral content of this photoluminescence is a direct measure of various important material properties.
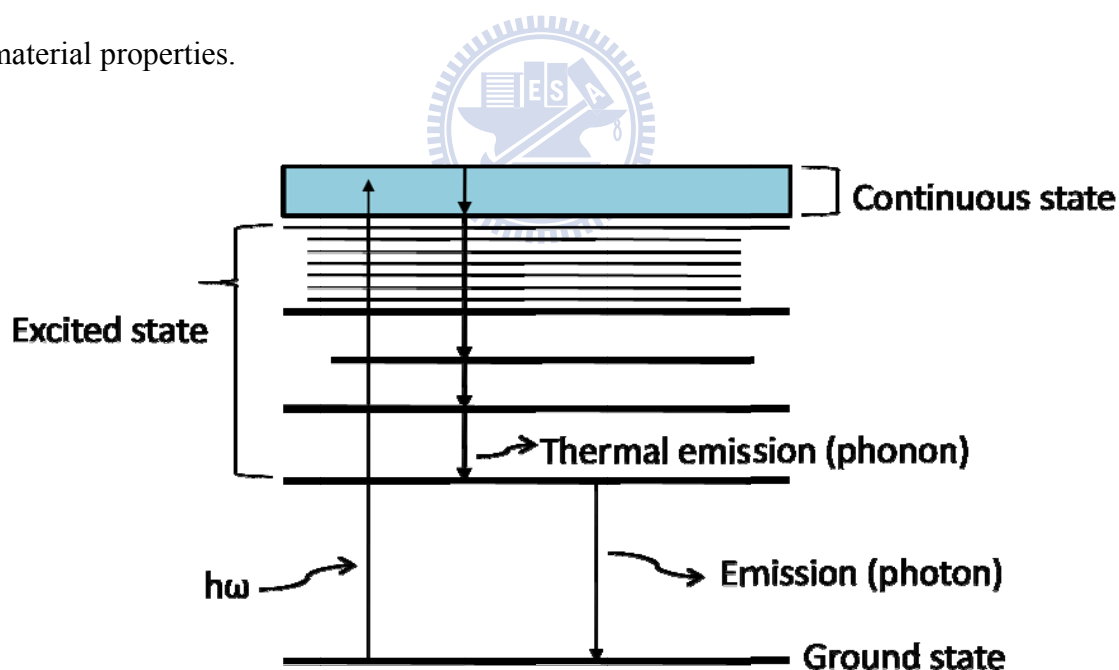

**Fig.3.20** Schematic of Electronic transition

   Photo-excitation causes electrons within the material to move into permissible excited states. When these electrons return to their equilibrium states, the excess energy is released and may include the emission of light (a radiative process) or may

44

not (a nonradiative process).

The energy of the emitted light (photoluminescence) relates to the difference in energy levels between the two electron states involved in the transition between the excited state and the equilibrium state. The quantity of the emitted light is related to the relative contribution of the radiative process.

Band Gap Determination

The most common radiative transition in semiconductors is between states in the conduction and valence bands, with the energy difference being known as the band gap. Fig.3.21 (a) (b) shows the optical absorption of the material for the direct and indirect bandgap. Electrons and holes will become free carriers in conduction band and valence band respectively.
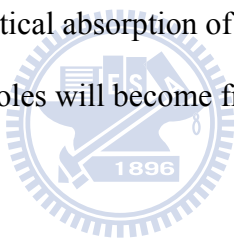
In fact, photoluminescence (Fig. 3.21 (c) (d)) can be treated as a radiation process due to the recombination of the electron in the conduction band and the hole in the valence band. When the excitation energy is less than the energy bandgap, the optical absorption will not occur. Band gap determination is particularly useful when working with new compound semiconductors.
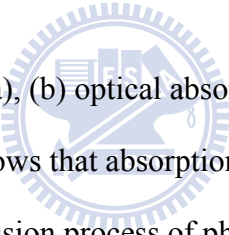
Fig. 3.21 Energy band diagram: (a), (b) optical absorption process and (c), (d) photoluminescence. Figure (b) shows that absorption process needs photon and phonon. Figure (d) show that emission process of photon and phonon. In an indirect energy gap material, the momentum conservation of phonon is considered.

Impurity Levels and Defect Detection

Radiative transitions in semiconductors also involve **localized defect levels (see fig.3.22)**. The photoluminescence energy associated with these levels can be used to identify specific impurity and defects, and the amount of photoluminescence can be used to determine their concentration. In general, nonradiative processes are associated with localized defect levels, whose presence is detrimental to material quality and subsequent device performance. Thus, material quality can be measured

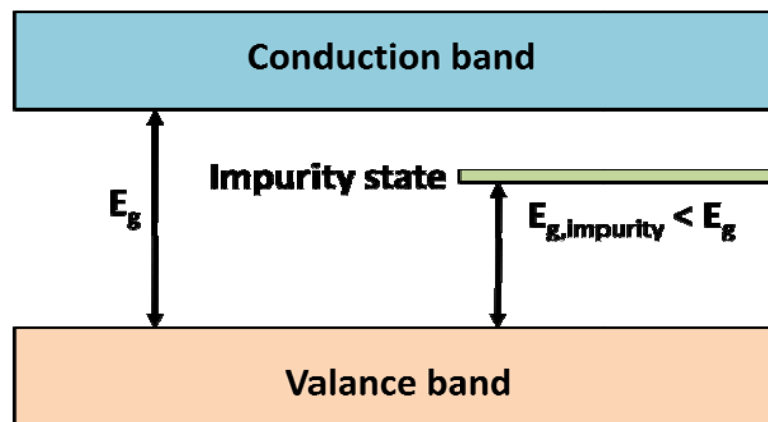by quantifying the amount of radiative recombination.

Fig.3.22 Energy difference caused by impurities

Recombination Mechanisms

The return to equilibrium, also known as "recombination," can involve both radiative (Fig.3.23) and nonradiative processes. The amount of photoluminescence and its dependence on the level of photo-excitation and temperature are directly related to the dominant recombination process. Analysis of photoluminescence helps to understand the underlying physics of the recombination mechanism.
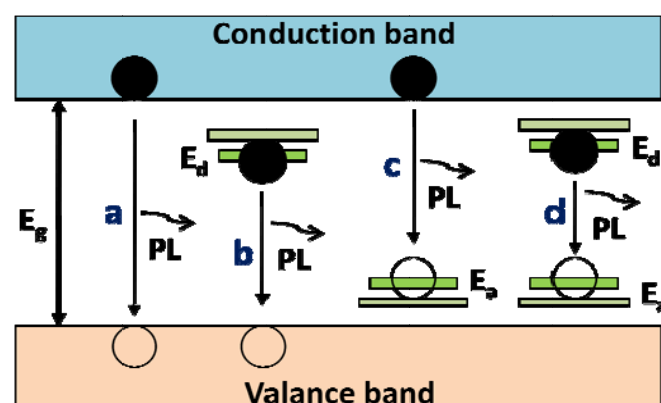

Fig.3.23 Radiative recombination paths: (a) band to band; (b) donor to valence band;

(c) conduction band to acceptor; (d) donor to accepter

Instrument

The samples were analyzed by micro-PL measurement on High Resolution Confocal Raman Microscope (Lab RAM HR Raman Microscope), we use both laser on He-Ne 632.8 nm wavelength and laser on diode pumped solid state (DPSS) 488 nm wavelength. (see Fig.3.11) Exposure time in all sample is keep the same as 10 sec to avoid noisy.

The illuminated spot size was about 10μm in diameter, and the power of the laser after multi-filtering was 15mW. Before measuring of the photoluminescence spectra, p-type Si substrate was used to calibrate the response signal on **488 nm** and **632 nm** respectively.

Quantum confinement effect in PL

In recent years, a great deal of research on Si NCs embedded in a silicon oxide matrix has been conducted because of their potential for applications in silicon-based optoelectronic devices. Silicon is characterized as having a very poor optical radiative efficiency and only produces light outside the visible range due to its indirect bandgap of 1.1eV. Silicon nanostructures show a quantum confinement effect which has an enhanced rate of electron–hole radiative recombination.

Fig. 3.24 [23] shows a room-temperature photoluminescence spectrum obtained from various sized Si NCs, where the tuning of the photoluminescence emission from 410 to 900 nm is possible by controlling the size of the Si NCs and, as a result, the emission color can be changed by controlling the size of the Si NCs.

Depending on the size, the photoluminescence of Si NCs can be tuned from the near infrared (1.38 eV) to the ultraviolet (3.02 eV).

Fig.3.24 Room-temperature PL spectra of Si NCs. The peak position can be controlled by appropriate adjustment of the nanocrystal size. [23]

The fitted photoluminescence peak energy as $E(eV)=1.16+11.8/d^2$ is evidence for the quantum confinement effect in Si NCs.(see Fig.3.25)[23]

Fig. 3.25 Photoluminescence peak energy of Si NCs as a function of crystal size. The

solid line was obtained from the effective mass theory for

three-dimensionally confined Si NCs. The dashed line was obtained from

the effective mass theory for amorphous silicon quantum dot structure in

Ref [24].

3-4.2 Experimental Results and Discussions

H-passivation and phase separation

After the experimental detail discussed, we are interesting in the passivation of impurities in the SRO/SiO$_2$ multilayer duo to the non-radiative defects exist in surface state and localize state. In Fig.3.26, we show the improvement of the PL intensity for the H-passivated sample. All H-passivated samples are under 500°C annealing with H$_2$ gas. It is found obviously that there is no change of the PL energy peak at about 1.465 eV and 1.646 eV. This result indicates that the main emission energy peak is not related to the interfacial region. Thus the PL energy peak is most likely caused by contributions from electron-hole recombination inside particular Si NCs of the appropriate size. Furthermore the results suggest that H-termination at the surface reduces the nonradiative recombination probability associated with surface defect states resulting in the improved PL intensity.
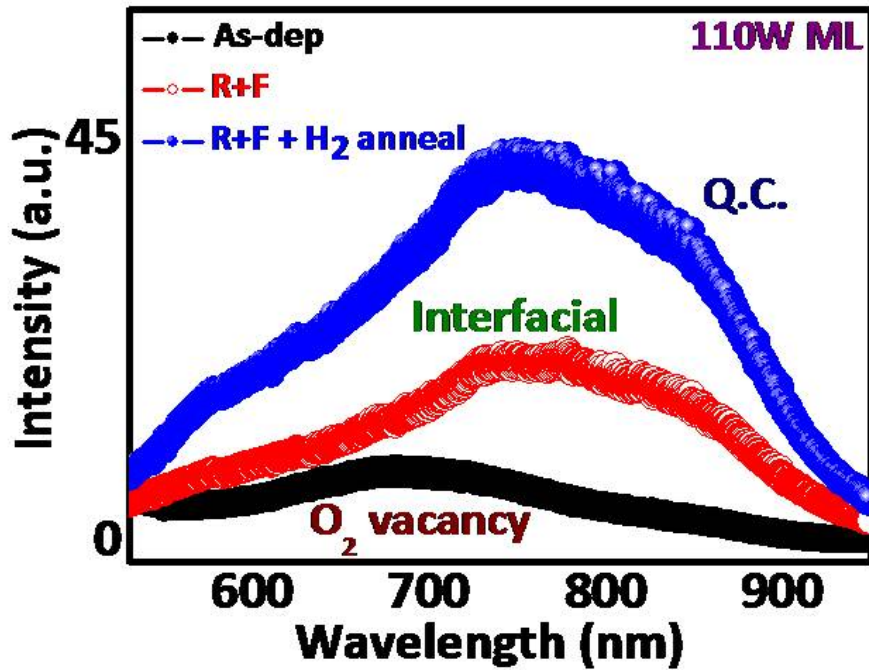
Fig. 3.26 Room temperature PL spectra of as-deposited sample and samples with and without H-passivation.

From the results of FTIR spectrum (Fig.3.4 to Fig.3.6), we also realize that phase separation in SRO/SiO₂ multilayer is achieved by thermal annealing process. The result is matched with the PL spectra, the black line depicted in Fig.3.26 shows the as-deposited films without any thermal annealing process, which has the main PL peak position located at about 690 nm (~1.797eV), this means the PL signal in as-deposited SRO/SiO₂ multilayer are a-Si dominated. After RTA 1050°C 30s and furnace 1100°C 1 hour, it's clearly show the peak red-shift and enhancement of the intensity of PL peak, the peak position are shift to 753 nm (~1.646eV) and 846 (~1.465) nm due to recombination in the interface of Si NCs and residual SiO₂ and quantum confinement effect in Si NCs.

51

Annealing condition dependence of PL spectra in Si NCs

Room temperature luminescence of Si NCs is not only related to three-dimensional quantum confinement [25],[26] but also determined by surface-related defects, surface passivation [27], oxidation effects [28],[29] and/or structural changes [30],[31]. Furthermore the existence of a suboxide shell around the Si NCs, and its influence on PL energy has been reported [25], [32], and [33].

Fig.3.27 and Fig.3.28show PL spectra of SRO/SiO$_2$ multilayer samples under different thermal annealing process, black line is the sample only under RTA 1050°C 30s process, the intensity of this samples are relative weak while the other two are about 5 to 10 times without H-passivation and 3 times with H-passivation in PL intensity.
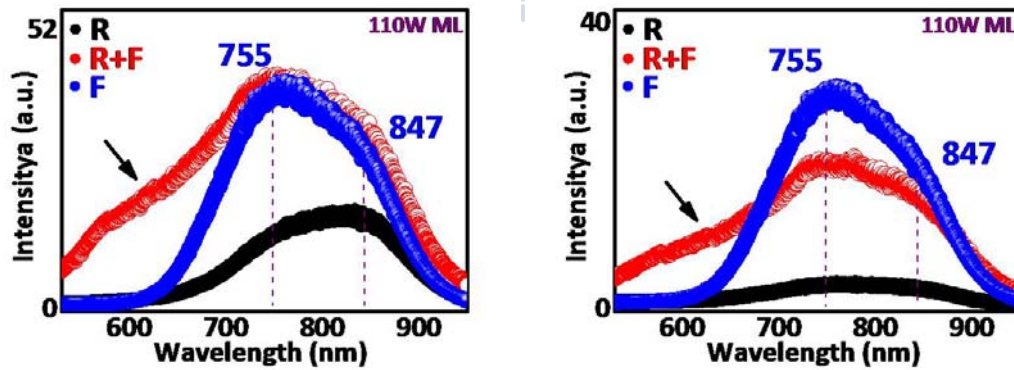

Fig.3.27, 28 PL spectra of SRO/SiO$_2$ multilayer under three thermal annealing process with (**left**) and without (**right**) H$_2$ gas.

To analyze the experimental data including chemical interface modeled such as a Si suboxide around Si NCs and defect states in the band gap of Si NCs, radiative

recombination in the O-passivated Si NCs corresponding to Si NC core, nonstoichiometric suboxide region around Si NCs, and oxygen vacancies localized close to the SiO$_2$ interface should be considered.[13]

To know more Si NCs-SiO$_2$ interface properties in Fig.3.27 and Fig.3.28, those PL spectra were demonstrated in terms of two or three Gaussian bands as a function of wavelength. Good curve fitting results were accomplished for the samples as shown in Fig.3.30 to Fig.3.35 and list at Table 3.7. We can clearly observed that all samples have two main Gaussian bands located at a range from 747 nm to 766 nm for the purple dash dot line and the others are from 842 nm to 860 nm for the blue dash line. There are the other PL spectra show Gaussian band located at 593 nm to 660 nm shown only in Fig.3.31, Fig.3.33 and Fig.3.34.

Table 3.7 List of peak position, intensity of PL under different annealing processes.

	W/WO H$_2$	1st Peak Intensity	2nd Peak Intensity	3rd Peak Intensity	1st Peak	2nd Peak	3rd Peak
Condition 1 (RTA)	WO H$_2$		2.43	0.96	×	758.25 nm (1.635 eV)	846.1 nm (1.46 eV)
	W H$_2$	0.99	12.64	11.93	660.49 nm (1.87eV)	766.66 nm (1.617 eV)	851.7 nm (1.45 eV)
Condition 2 (RTA+Furnace)	WO H$_2$	8.21	13.72	10.38	651 nm (1.9 eV)	757.75 nm (1.636 eV)	849.4 nm (1.46 eV)
	W H$_2$	10.80	39.54	10.93	593.79 nm (2.09eV)	754.31 nm (1.643 eV)	860 nm (1.44 eV)
Condition 3 (Furnace)	WO H$_2$		28.84	12.53	×	749.7 nm (1.653 eV)	846.35 nm (1.46 eV)
	W H$_2$		38.28	21.21	×	747 nm (1.659 eV)	842.8 nm (1.47 eV)

Table 3.8 lists the main recombination processes of different emission wavelength. The peak position located at a range from 704 nm (1.76 eV) to 783 nm (1.58eV) are possibly attributed to recombination in the interfacial region, which are between Si NCs and suboxide shell, the fixed oxide charges due to polar bonding are assumed to be located very close to the Si NC-SiO$_2$ interface. This charge is related to allowed states in the oxide or oxygen vacancies, which are above the oxide valence band about 6.3 eV [34]. Hence those O-vacancy states are constant in energy because it is insensitive to the position of the Fermi level at the Si-SiO$_2$ interface [35]. In low-dimensional systems, the energy of radiative recombination probability due to oxygen vacancies should be 1.60 eV + ΔE_v as shown in Fig.3.29 [13]. Since ΔE_v the first quantized energy level in the valence band is small, the possible energy of radiative recombination at the interfacial region is between 1.60 eV and 1.70 eV, approximately.

Table 3.8 Relation between PL emission range and recombination mechanism.

Oxygen vacancy, S==O double bond	< 700 nm (>1.77eV)
Interfacial region	704 – 783 nm (1.583-1.76eV)
Quantum confinement effects	763 – 892 nm (1.39-1.625eV)
Localized state recombination	832 – 967 nm (1.282-1.49eV)

The peak positions located at a range from 763 nm (1.625 eV) to 892 nm (1.39eV) are due to quantum confinement effect in the Si NCs. Radiative recombination from impurities in SiO shell are thought to be the localized state, which has a range from 832 nm (1.49 eV) to 967 nm (1.282 eV).
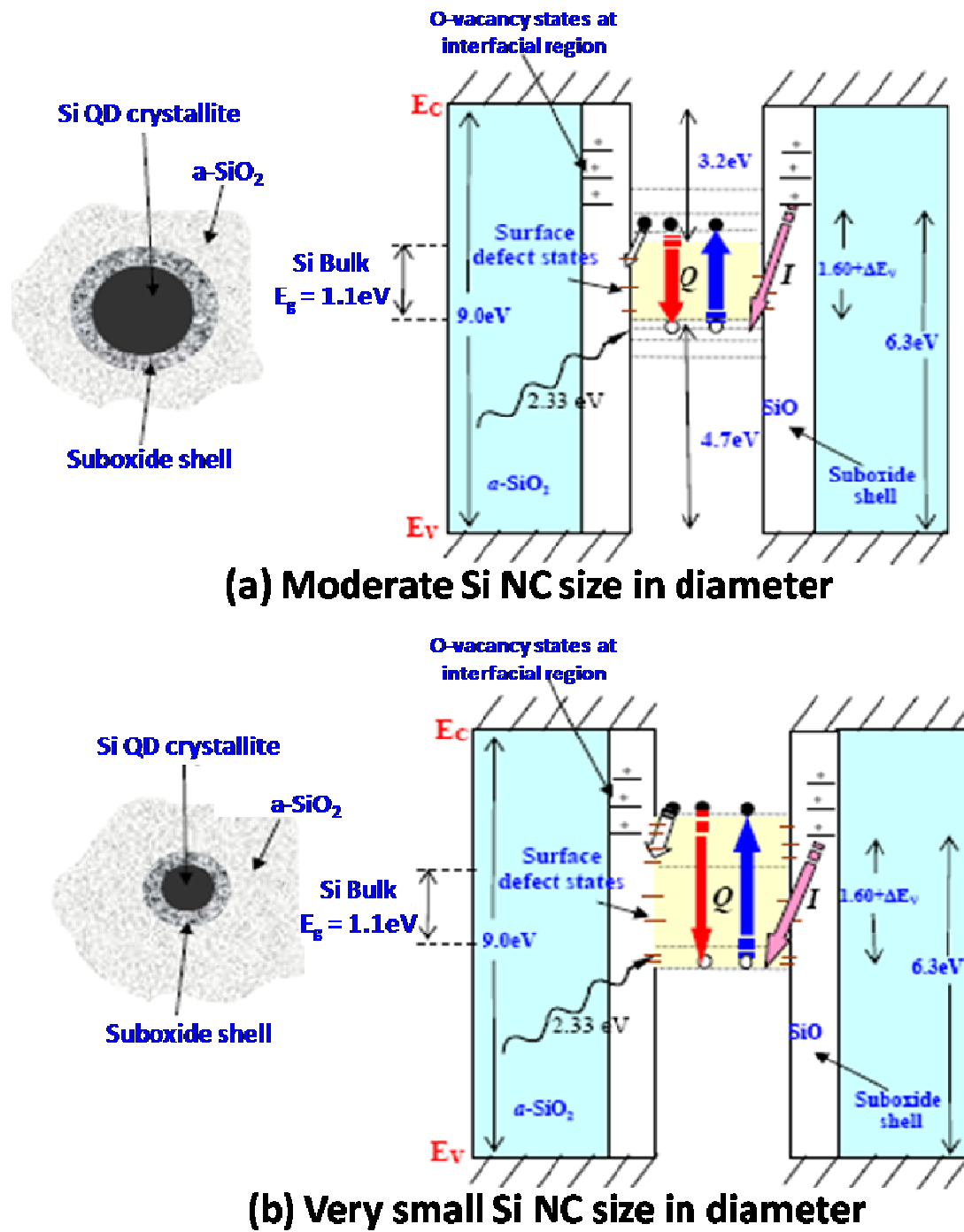
Fig.3.29 Schematic illustration of an interface model of photoluminescence predominantly based on the quantum confinement effect in the case of (a) moderate and (b) very small SiQDs (not to scale and band-bending effects not shown).
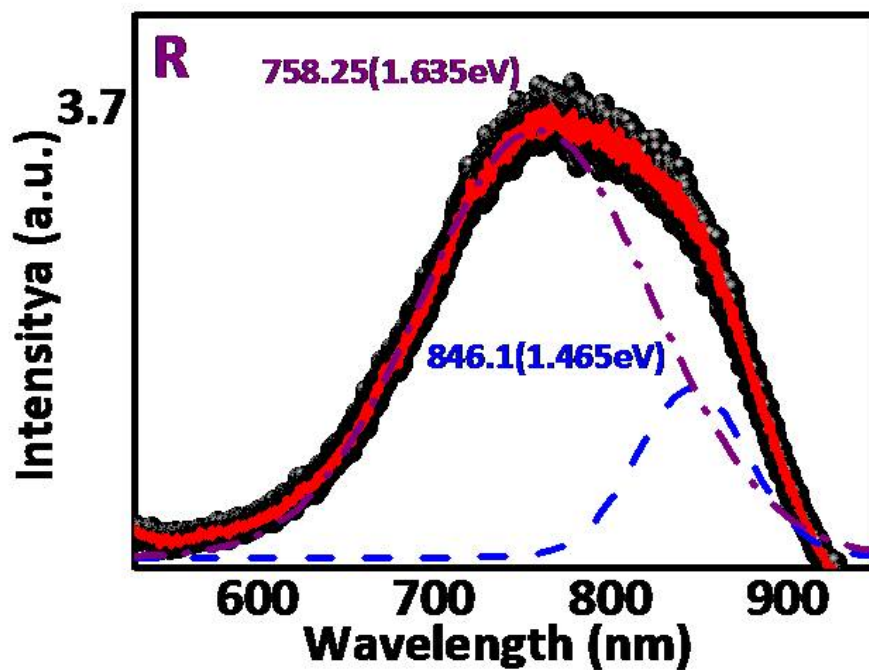
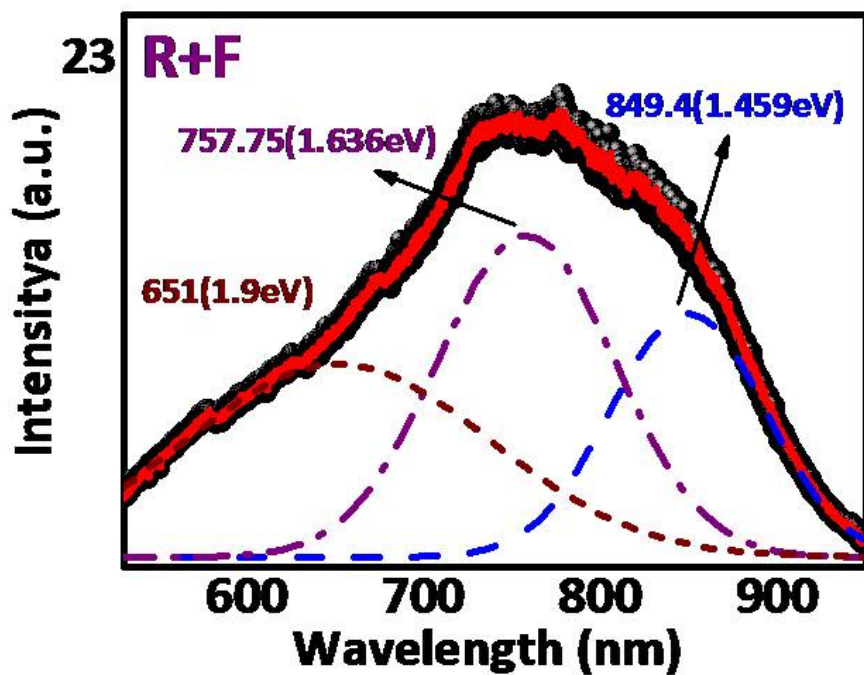**Fig.3.30** PL spectra of SRO/SiO$_2$ multilayer under condition 1 process without H$_2$.

Fig.3.31 PL spectra of SRO/SiO$_2$ multilayer under condition 2 process without H$_2$.
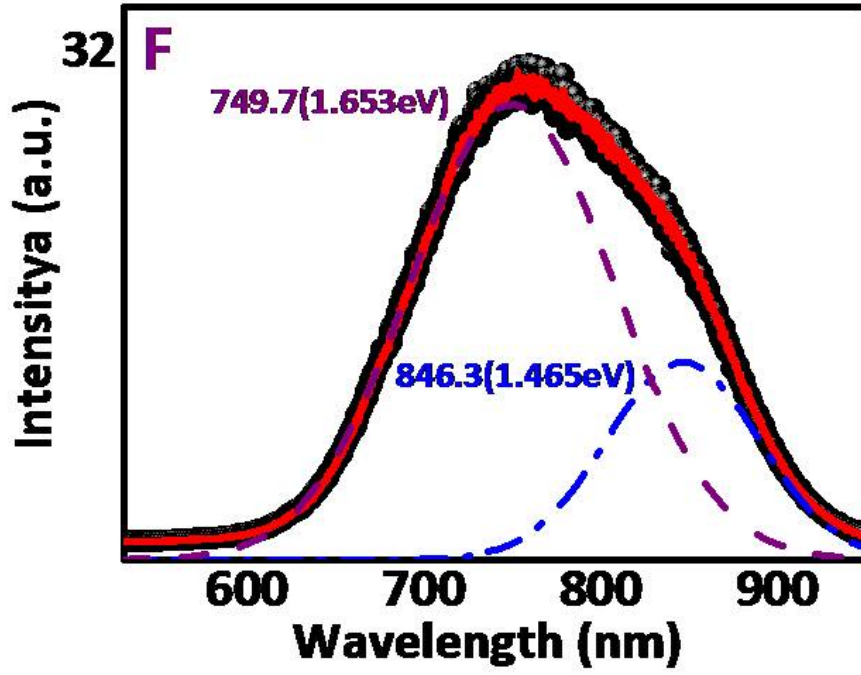
Fig.3.32 PL spectra of SRO/SiO$_2$ multilayer under condition 3 process without H$_2$.
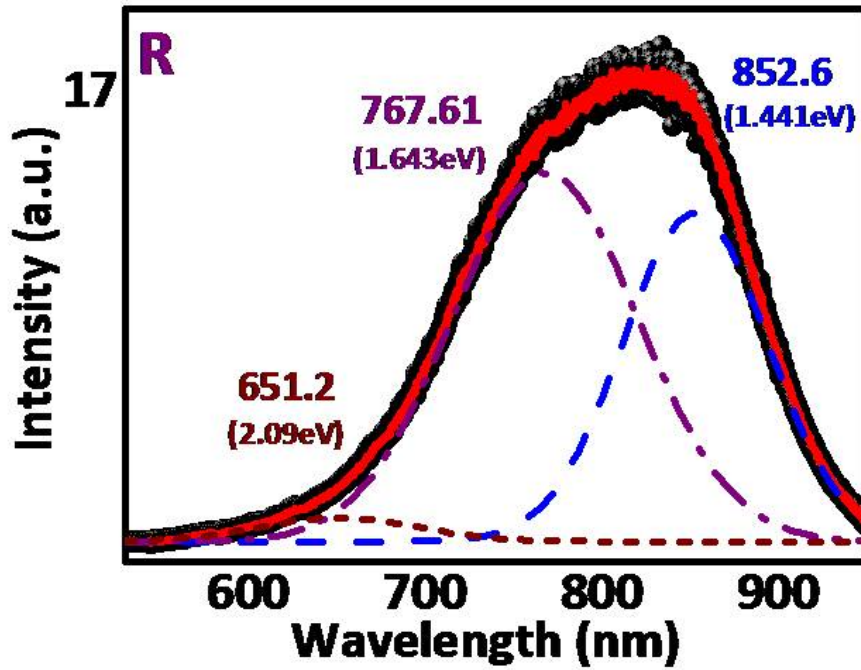

Fig.3.33 PL spectra of SRO/SiO$_2$ multilayer under condition 1 process with H$_2$.
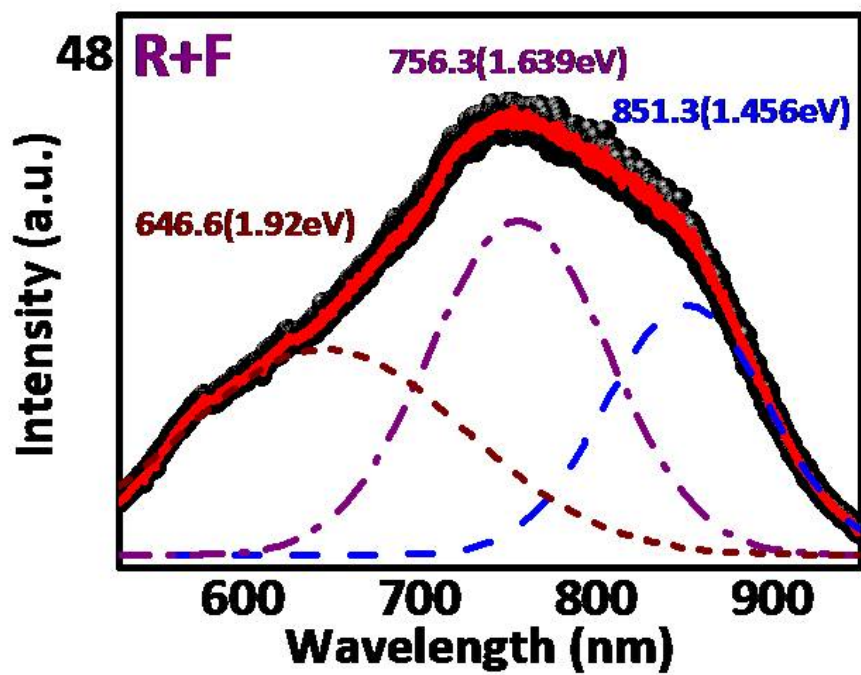
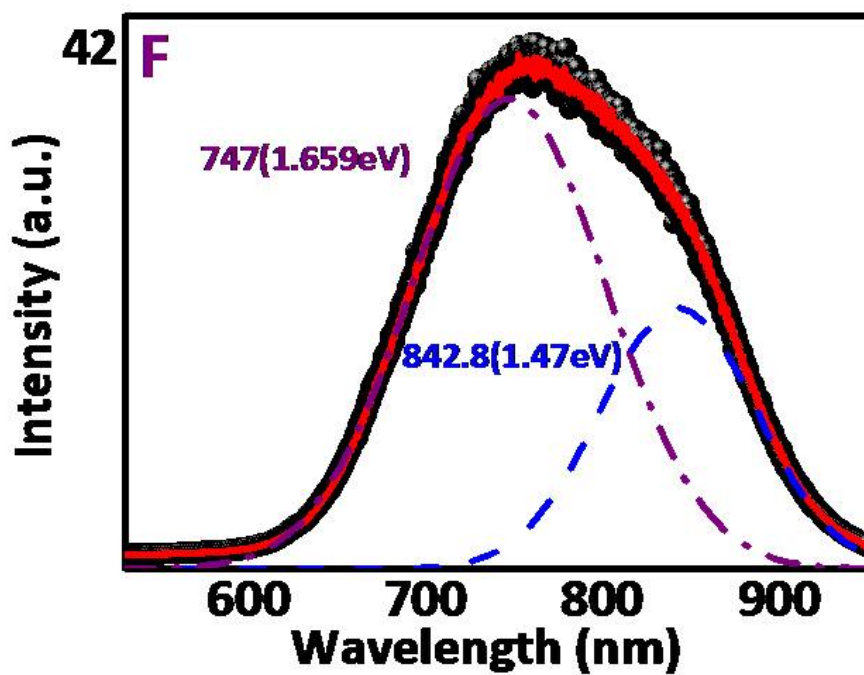**Fig.3.34** PL spectra of SRO/SiO$_2$ multilayer under condition 2 process with H$_2$.

Fig.3.35 PL spectra of SRO/SiO$_2$ multilayer under condition 3 process with H$_2$.

Peak position from 593 nm (2.09 eV) to 660 nm (1.878eV) might due to the defects and impurities of the bandgap between Si and SiO$_2$, amorphous Si, Si=O double bond, and other oxygen vacancy. In Fig.3.31, there is no Gaussian band fitted in this range due to RTA 1050°C 30s process seems to product nonradiative recombination defects in our structure, sequentially, as Fig.3.31 shown, after furnace 1100°C 1 hour, this band becomes emission because those defects are passivated. This result also happen in the sample during H-passivated (Fig.3.33).

Fig.3.32 and Fig3.35 show PL spectra of the sample under furnace 1100°C 1 hour, it's obviously show that there are no signal from 593 nm to 660 nm, it may attributed to good passivation in oxygen vacancy and impurities during furnace process only.

In chapter 3.2, we discuss the temperature condition dependence of Raman spectra, from the Raman spectra; we realize the volume fraction of crystalline of sample under RTA is not as good as the sample under RTA and Furnace or only Furnace. From Table 3.7 and Fig.30-32 we calculate the ratio of relative intensity from interface region (704 nm – 783 nm) and quantum confinement of Si NCs (763 nm – 892 nm), the ratios from condition 1to condition 3 are 2.5626, 1.321 and 1.359 respectively. This result is matched with the result from annealing condition dependence of Raman spectra.

Size dependence of PL spectra in Si NCs

In this section, we focus on the size dependence of the PL spectra in Si NCs, the main difference is the thickness of the SRO films are 2.5nm, 5nm, 10nm for each SRO/SiO$_2$ multilayer respectively but keeps total thickness of each SRO/SiO$_2$

multilayer the same. Fig.3.36 shows the size dependence of PL spectra under RTA 1050°C 30s processes and furnace 1100°C 1 hour processes sequentially. From Fig.3.36, the blue shift of peak is observed as the thickness of the SRO decrease. This might come from the radiative recombination from oxygen-related localized states, the S==O double bond [27]. S==O double bond will produce localized levels in the bandgap of Si NCs. The PL spectra on multilayer structure with 10 nm in each SRO film shows no emission from S==O due to the main mechanism of recombination is from free exciton in Si NCs and interface between Si NCs and SiO$_2$ matrix. To understand more information, the detailed curve fitting are shown as Fig.3.37-39 and list in Table 3.9
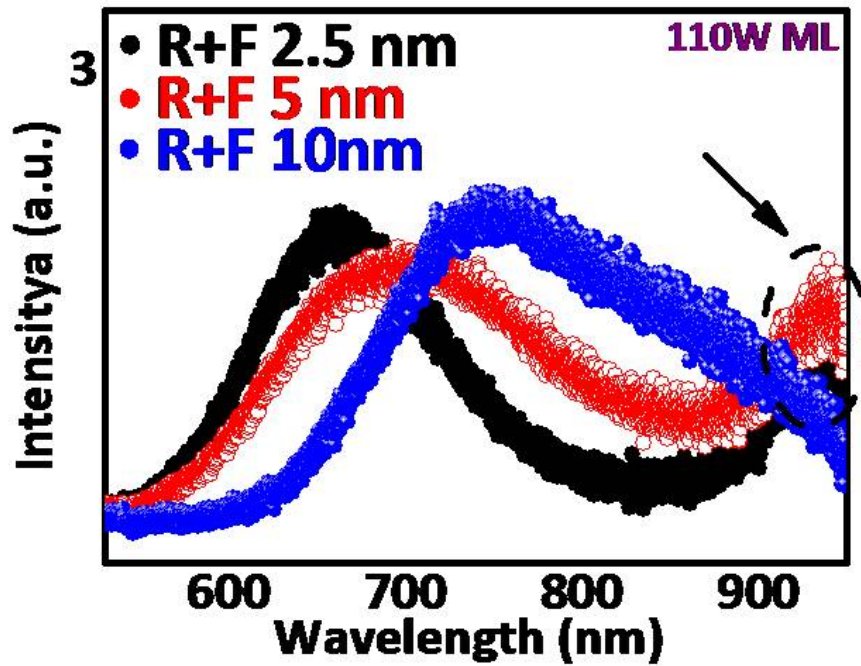

Fig.3.36 Size dependence of PL spectra under RTA 1050°C 30s and Furnace 1100°C 1hour processes.

Table 3.9 List of PL spectra depend on different SRO thickness.

	Oxygen vacancy Peak (nm)	Interfacial region Peak (nm)	Q.C. Peak (nm)	Localized state S==O Peak (nm)
2.5 nm	651.3 (1.90 eV)	716.9 (1.73 eV)	787.2 (1.575eV)	946.7 (1.31 eV)
5 nm	651.3 (1.90 eV)	723.2 (1.71 eV)	832.9 (1.488eV)	945.7 (1.30 eV)
10 nm	651.0 (1.90 eV)	743.5 (1.67 eV)	850.3 (1.458 eV)	NA

From Table 3.8 and Table 3.9 we notice that the signal of oxygen vacancy is all located in 651 nm. When we decrease the thickness of SRO film, the blueshift from interfacial region and quantum confinement are obviously observed. This is because the energy states are discrete to higher state in conduction band as decrease the thickness of SRO film. The PL peaks located at a range from 928.43 to 954.48 nm are come from the localized states in the bandgap.
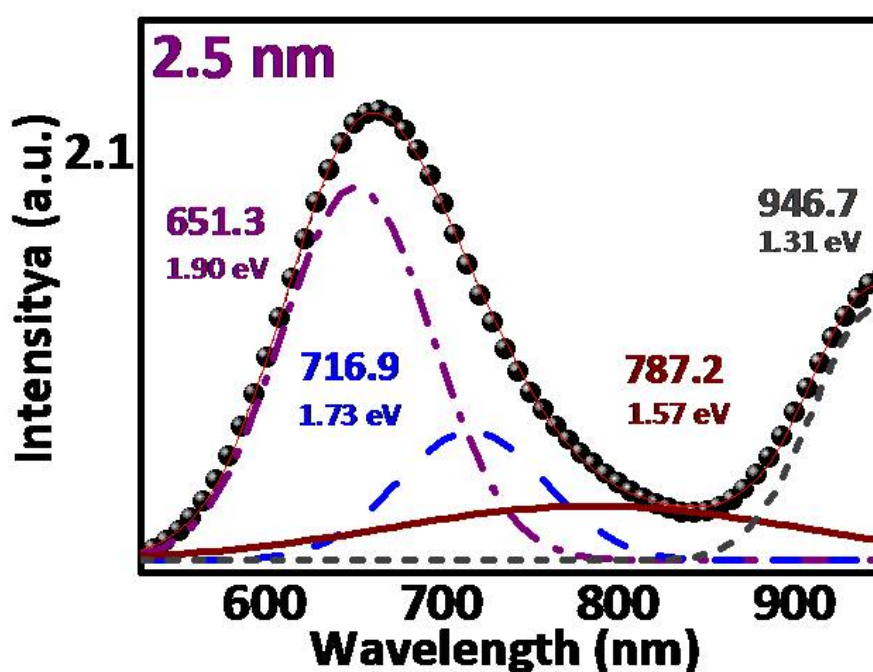

Fig.3.37 Measured and decomposed PL spectra of SRO/SiO$_2$ (2.5nm/5nm) multilayer.
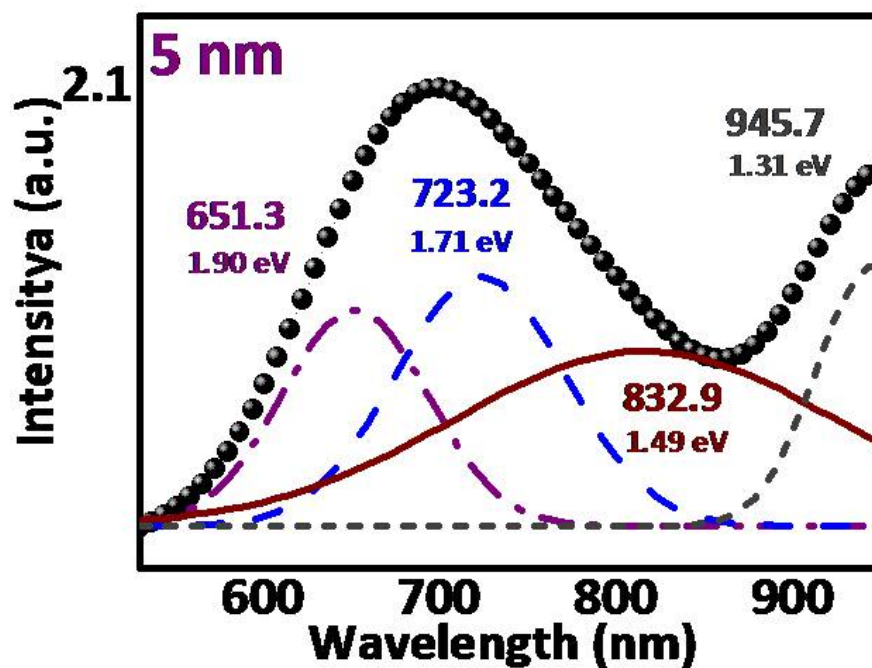
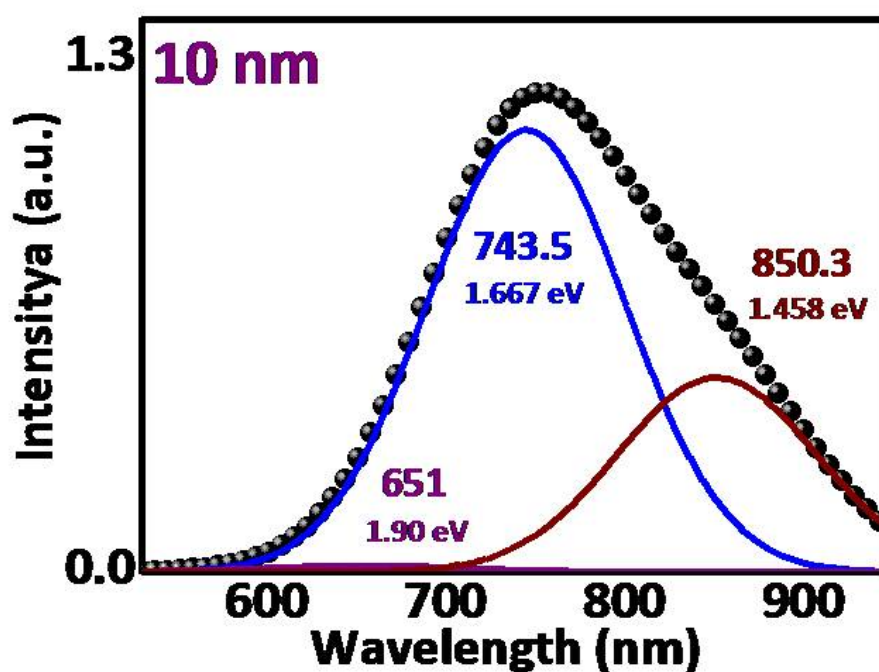**Fig.3.38** Measured and decomposed PL spectra of SRO/SiO$_2$ (5nm/5nm) multilayer.

Fig.3.39 Measured and decomposed PL spectra of SRO/SiO$_2$ (10nm/5nm) multilayer.

3-5 Summaries

From FTIR spectroscopy, we confirm that the phase separation exactly happened when as-deposited SRO/SiO$_2$ multilayer under high temperature annealing. The peak shift is clearly shown in Fig.3.7.

From thermal condition dependence of Raman spectra, different thermal annealing condition are compared, from Table 3.3, we calculated the critical volume fraction of crystalline of the sample under RTA process is 78% which value is lower than the other two thermal annealing conditions (RTA with Furnace and Furnace only). These results are well-matched with the Raman and PL spectra.

We also investigate the size dependence of PL spectra. Blue shift of PL energy is also observed in PL spectra. By fitting the PL curve, we know the Si==O double bond are present in our structure when size of Si NCs small than 5 nm, and the recombination from interface states between Si NCs and SiO$_2$ matrix are located at a range from 727.45 to 778.79 nm; PL peak from 763 to 892 nm are due to recombination from quantum confinement effect, and recombination from localized states and S==O in bandgap are probably located from832 to 967 nm.

Chapter 4. Photovoltaics Property

4-1. Properties of multilayer structures on Vertical Electrode

Fabrication procedure of vertical electrode

Step1. Spin coating (positive photoresister) and Exposure

In the beginning, we first design a mask with 16 square patterns, as shown in Fig.4.1, and then, photoresister are spin coat on our multilayer by using these 16 square patterns due to isolate the surrounding patterns.
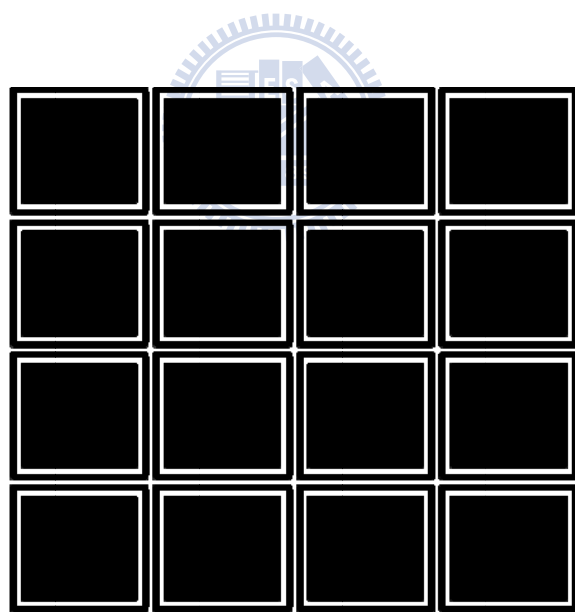

Fig.4.1 Schematic of the 16 square patterns mask

Fig.4.2 After exposure 70 s and photolithography process.

Step2. (Reactive Ion Etcher) RIE

As Fig.4.2 show, those black patterns are stick on our multilayer, the subsequent

reactive ion etching process is applied on the sample to etch the region without black

patterns (see Fig.4.3). The reactive gas during etching is O_2 and CHF_3. The purpose of

RIE is to isolate each pattern to other patterns for better yield rate in electrical

measurement.

Fig.4.3 After RIE, the isolated multilayer is cover with a thin photoresister.

Step3. Spin coating (positive photoresister) and Exposure

After RIE, we again spin coating positive photoresister on our multilayer with 16 finger-like patterns mask (see Fig.4.4).
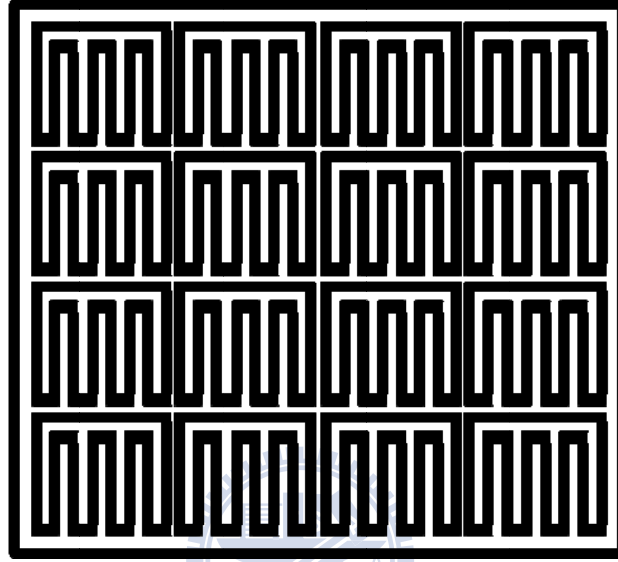

Fig.4.4 The 16 upper finger-like patterns mask.

Step4. Thermal coater for electrode

After exposure and fixed, Ni and Al are coating on the top and bottom as the top and bottom electrode of the sample, we should notice that the Ni is full of whole region including the place which un-sensitive of photoresister.

Step5. Lift-off

When we finish the Ni coating, we put the sample in acetone, by using the sonic approach to lift off the residual photoresister, the left part is show the finger-like electrode (see Fig.4.5).
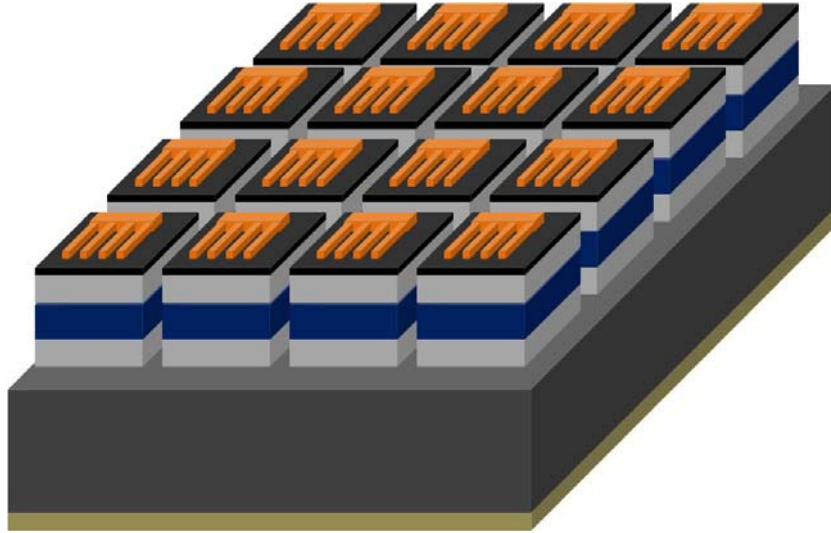
Fig.4.5 After lift-off, the top 16 electrodes are lift on the multilayer.

Electrical propriety on SRO/SiO₂ multilayer

In this part, we change the thickness of each SRO film but keep all thickness of multilayer the same. The thickness of SRO films (5 nm and 10 nm) is depicted as Fig4.6 and Fig4.7. From Fig4.6 and Fig4.7, we can see the property of photodector on reverse bias side, which might because the quantum confinement. But in the 2.5 nm case, we see no photodector properties due to the total thickness of oxide films are too thick.
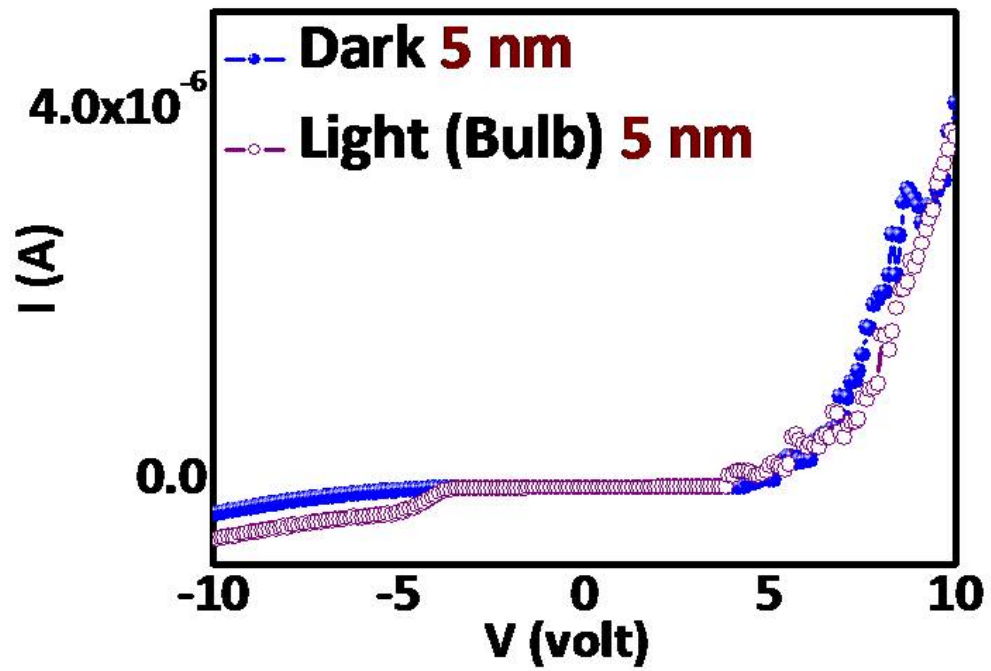
Fig.4.6 The I-V curve on 5nm/5nm SRO/SiO$_2$ multilayer.

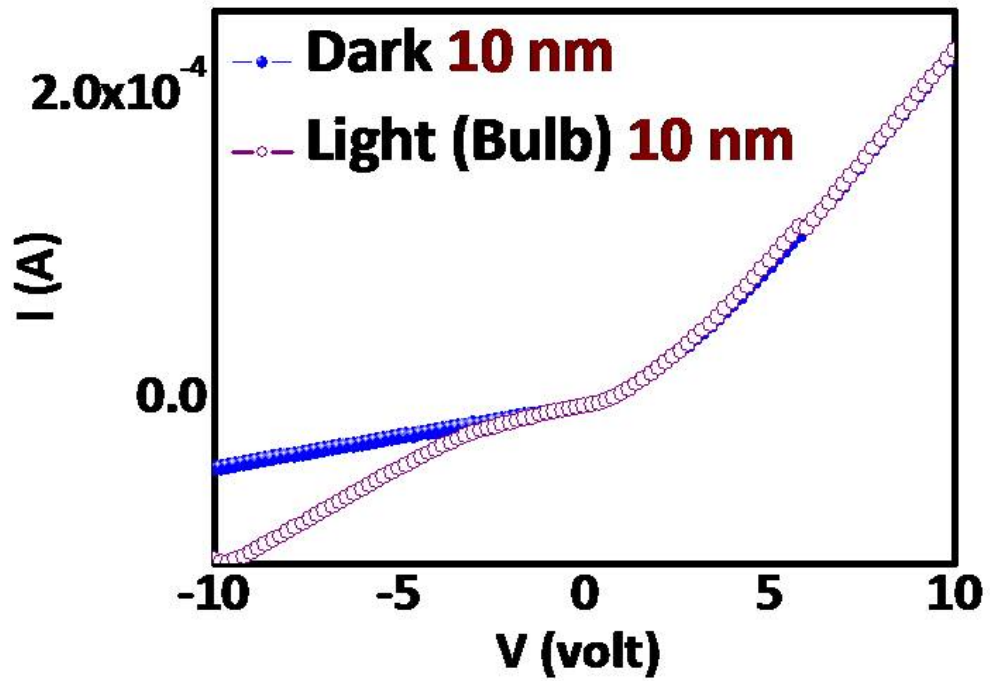**Fig.4.7** The I-V curve on 10nm/5nm SRO/SiO$_2$ multilayer.

4-2. Summaries

From the I-V curves, we see the property of photodetector from two different thicknesses (5 nm and 10 nm) of SRO/SiO_2 multilayer but no photodetector property on 2.5nm, this might because the thickness of SiO_2 are too thick to transport the carrier. The reason for no photovoltaic is due to the thick thickness on SiO_2.

Chapter 5. Conclusions and future work

5-1. Conclusions

In this thesis, RF magnetron co-sputtering provided the capability of creating superlattice structures in conjunction with high temperature annealing, to form Si NCs in an oxide matrix.

Generally speaking, this thesis investigated the structural, optical and electrical properties of Si nanocrystals multilayer in order to expand the application of luminescence and electrical efficiency. Several structural characterization techniques, such as FTIR, Raman spectroscopy, RT PL and TEM have been applied to this study since each individual technique has inherent limitations for accurately examining ultra small Si NCs.

For SRO single film, results from TO mode frequency measurements by using FTIR addressed that the high temperature annealing at 1100°C 1 hour and 1050°C 30 s strongly shifts peak position of T_3O mode to higher wavenumbers at 1089 cm^{-1} and 1076 cm^{-1} respectively. Meanwhile, the annealing heat treatment more or less enhances their peak intensity. The results can be represented the phase separation of Si and SiO$_2$ due to the corresponding absorption peak of thermal SiO$_2$.

In addition, from Raman spectra measurement, the existence of crystalline Si NCs can be confirmed by appearance of first-order TO Raman spectra, indicating a sharp peak at position near 515 cm^{-1} and 518 cm^{-1} at different thermal annealing process.

Furthermore, Si NCs embedded in dielectric matrices has attracted a significant amount of attention due to the potential to increase the bandgap of Si due to quantum confinement effects. In this thesis, the PL results have clearly shown that the phase separation during RTA 1050°C 30s and furnace 1100°C 1 hour, the peak position located at a range from 747 nm (1.659 eV) to 766 nm (1.618eV) are possibly attributed to recombination in the interfacial region, which are between Si NCs and suboxide shell. The peak positions located at a range from 842 nm (1.472 eV) to 860 nm (1.441eV) are due to confinement effect in the Si NCs. Peak position from 593 nm (2.09 eV) to 660 nm (1.878eV) might due to the presence of S==O double bond which produced localized levels in the bandgap of Si NCs smaller than 3nm.

We see no property of photodetector on 2.5nm but 5nm and 10 nm. It might suggest that the thickness of SiO_2 is too thick to conduct.

5-2. Future work

To achieve Tandem cell, optical gap and crystallinity on size dependence of Raman and PL need more investigation. We might **reduce the thickness of SiO_2** to enhance carrier tunneling probability in the oxide matrix. The mechanism of carrier transport might correlated with oxygen vacancy, to achieve a better transport mechanism, we can try to realize more detail information about this. Besides the vertical electrode, **lateral electrode** might be the other approach to improve the conductivity.

Reference

[1]. J. Zhao, A. Wang, M.A. Green, F. Ferrazza, "19.8% efficient "honeycomb" textured multicrystalline and 24.4% monocrystalline silicon solar cells," *Appl. Phys. Lett.* 73, 1991 (1998).

[2]. M. A. Green, "Crystalline and thin-film silicon solar cells: state of the art and future potential," *Solar Energy*, 74, 181 (2003).

[3]. M. A. Green, "Third Generation Photovoltaics: Ultra-high Conversion Efficiency at Low Cost" *Progress In Photovoltaics: Research and Applications 9:123-135* (2001).

[4]. Gavin Conibeer , Martin Green, Eun-Chel Cho, Dirk König, Young-Hyun Cho, "Silicon quantum dot nanostructures for tandem photovoltaic cells" Thin Solid Films (2008).

[5]. M.A. Green "Third Generation Photovoltaics" Advanced Solar Energy Conversion, Springer (2006)

[6]. A. Marti, G.L. Araujo, Sol. Energy Mater. Sol. Cells 43, 203 (1996)

[7]. M. A. Green, E-C. Cho, Y. Cho, Y. Huang, E. Pink, T. Trupke, A. Lin, T. Fangsuwannarak, T. Puzzer, G. Conibeer, and R. Corkish, "All-silicon tandem cells based on "Artificial" semiconductor synthesised using silicon quantum dots in dielectric matrix," *The 20th European Photovoltaic Solar Energy Conference and Exhibition, Dresden* (2006).

[8]. G. Scardera, T. Puzzer, D. McGrouther, E. Pink, T. Fangsuwannarak, G. Conibeer, and M. A. Green, " Investigating Large Area Fabrication if Silicon Quantum dots in a Nitride Matrix for Photovoltaic Applications" , *IEEE World Conference on Photovoltaic Energy Conversion,* Hawaii, 122 ,(2006).

[9]. Green, M.A., Cho, E.-C., Cho, Y., Huang, Y., Pink, E., Trupke, T., Lin, A.,

"All-Silicon Tandem Cells Based On "Artificial" Semiconductor Synthesized Using Silicon Quantum Dots In a Dielectric Matrix " 20th European Photovoltaic Solar Energy Conference, 6 – 10 (2005)

[10]. Y.M. Niquet, C. Delerue, G. Allan and M. Lannoo, Phys. Rev. B62, 5109 (2000).

[11]. M. Zacharias, J. Heitmann, R. Scholz, U. Kahler, M. Schmidt, and J. Bläsing, Appl. Phys. Lett. **80**, 661 (2002).

[12]. J.U. Schmidt 1,*, B. Schmidt "Investigation of Si nanoclusters formation in sputter-deposited silicon sub-oxides for nanoclusters memory structures" Materials Science and Engineering (2003).

[13]. Thipwan Fangsuwannarak," Electronic and Optical Characterisations of Silicon Quantum Dots and its Applications in Solar Cells " April (2007)

[14]. Z. Yu, M. A. Mijares, E. Quiroga, R. L. Estopier, J. Carrillo, and C. Falcony, "Structural and optical properties of Si/SiO_2 superlattices prepared by low pressure chemical vapor deposition," *J. Appl. Phys.* 100, 013524 (2006).

[15]. Jiwang Yan, Tooru Asami, Tsunemoto Kuriyagawa" Nondestructive measurement of machining-induced amorphous layers in single-crystal silicon by laser micro-Raman spectroscopy", Precision Engineering **32** 186–195 (2008).

[16]. C. V. Raman, and K. S. Krishna , " A new type of secondary radiation," Nature 121, 501 (1928).

[17]. Zwick A, Carles R. Multiple-order Raman scattering in crystalline and amorphous silicon. Phys Rev B 1993;48(9):6024–32.

[18]. R. Tsu, J. Gonzalez-Hernandez, S. S. Chao, S. C. Lee, and K. Tanaka , "Critical volume fraction of crystallinity for conductivity percolation in phosphorus-doped

Si:F:H alloys," Appl. Phys. Lett. 40, 534 (1982).

[19]. Shihua Huang, Hong Xiao, Sha Shou" Annealing temperature dependence of Raman scattering in Si/SiO$_2$ superlattice prepared by magnetron sputtering" Applied Surface Science, **255,** (2009), 4547-4550.

[20]. H. Richter, Z.P. Wang, L. Ley, Solid State Commun. **39**, 625 (1981)

[21]. Jian Zi, Kaiming Zhang, Xide Xie, Phys. Rev. B **55**, 9263(1997)

[22]. G. Faraci1,a, S. Gibilisco1, P. Russo1, A.R. Pennisi1, G. Compagnini2, S. Battiato2, R. Puglisi3, and S. La Rosa   "Si/SiO2 core shell clusters probed by Raman spectroscopy" Eur. Phys. J. B **46**, 457–461 (2005).

[23]. Tae-Youb Kim, Nae-Man Park, Kyung-Hyun Kim, and Gun Yong Sung, " Quantum confinement effect of Si NCs in situ grown in silicon nitride films", Appl. Phys. Lett. **85**, 22, (2004)

[24]. N.-M. Park, C.-J. Choi, T. Y. Seong, and S.-J. Park, Phys. Rev. Lett. **86**, 1355 (2001).

[25]. Y. Kanemitsu, T. Ogawa, K. Shiraishi, and K. Takeda, "Visible

PL from oxidized Si nanometer-sized spheres: Exciton confinement

on a spherical shell ," *Phys. Rev. B* 48 4883 (1993)

[26]. S. Schuppler, S. L. Friedman, M. A. Marcus, D. L. Adler, and Y.-H. Xie, "Size,

shape, and composition of luminescent species in oxidized Si nanocrystals and

H-passivated porous Si," Phys. Rev. B *52, 4910 (1995)*.

[27]. M. V. Wolkin, J. Jorne, P. M. Fauchet, G. Allan, and C. Delerue, "Electronic

states and luminescence in porous silicon quantum dots: The role of oxygen," Phys.

Rev. Lett. *82, 197 (1999)*.

[28]. J. S. Biteen, N. S. Lewis, H. A. Atwater, and A. Polman, "*Size-dependent oxygen-related electronic states in silicon nanocrystals* ," Appl. Phys. Lett*. 84, 5389 (2004)*.

[29].X. Y. Chen, Y. F. Lu, L. J. Tang, Y. H. Wu, B. J. Cho, X. J. Xu, J. R. Dongt, and W. D. Song, "Annealing and oxidation of silicon oxide films prepared by plasma-enhanced chemical vapor deposition,"J. Appl. Phys*. 97, 014913 (2005)*.

[30]. H. Hofmeister and P. Ködderitzsch, "Nanosized silicon particles by inert gas arc evaporation," *Nanostructured Materials* 12, 203, (1999).

[31]. G. Ledoux, O. Guillois, D. Porterat, C. Reynaud, F. Huisken, B. Kohn, and V. Paillard, "Photoluminescence properties of silicon nanocrystals as a function of their size," Phys. Rev. B *62, 15942 (2000)*.

[32]. D. Kovalev, H. Heckler, B. Averboukh, and F. Koch, "Breakdown of the k-conservation rule in Si nanocrystals," Phys. Rev. B *57,3741 (1998*).

[33]. N. Daldosso, M. Luppi, S. Ossicini, E. Degoli, R. Magri, G. Dalba, P. Fornasini, R. Grisenti, F. Rocca, L. Pavesi, S. Boninelli, F. Priolo, C. Spinella, and F. Iacona, **"**Role of the interface region on the optoelectronic properties of silicon nanocrystals embedded in SiO_2," Phys. Rev. B *68, 085327 (2003)***.**

[34]. M. A. Green, *Silicon Solar Cells: Advanced Principles &Practice*, Center for Photovoltaic Devices and Systems, University of New South Wales, 1995.

[35]. A. G. Aberle, *Crystalline Silicon Solar cells: Advanced Surface Passivation and Analysis,* Center for Photovoltaic Devices and Systems, University of New South Wales, 1999.